Cell Reports

Article

Excessive E2F Transcription in Single Cancer Cells Precludes Transient Cell-Cycle Exit after DNA Damage

Graphical Abstract

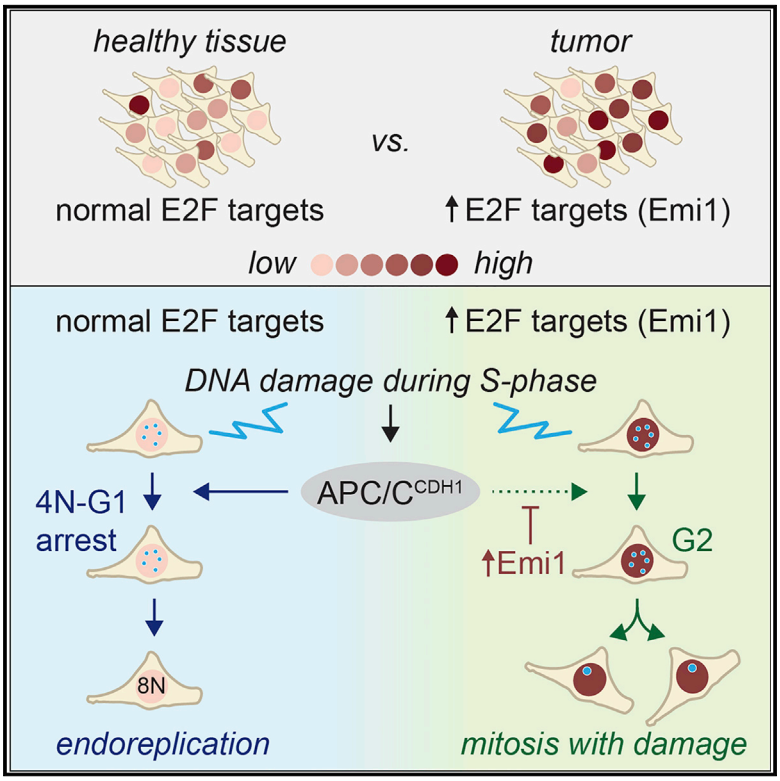

Highlights

- Individual cycling cancer cells display enhanced E2F target gene expression
- E2F7/8 deletion or E2F3 overexpression overrides cell-cycle exit after DNA damage
- Elevated levels of the E2F target Emi1 prevent DNA-damage-induced cell-cycle exit
- The cell-cycle exit after DNA damage is transient and leads to endoreplication

Authors

Hendrika A. Segeren, Lotte M. van Rijnberk, Eva Moreno, ..., Richard Wubbolts, Alain de Bruin, Bart Westendorp

Correspondence

b.westendorp@uu.nl

In Brief

Segeren et al. demonstrate that cycling human cancer cells exhibit abnormally high E2F target gene expression. Healthy cells can activate APC/C^{Cdh1} after DNA damage to allow a transient cell-cycle exit. However, elevated transcription of the E2F target Emi1 forces cells to progress to mitosis and potentially promotes genomic instability.

Segeren et al., 2020, Cell Reports *33*, 108449
December 1, 2020
https://doi.org/10.1016/j.celrep.2020.108449

CellPress

Cell Reports

CellPress
OPEN ACCESS

Article

Excessive E2F Transcription in Single Cancer Cells Precludes Transient Cell-Cycle Exit after DNA Damage

Hendrika A. Segeren,[1] Lotte M. van Rijnberk,[1,4] Eva Moreno,[1] Frank M. Riemers,[1,2] Elsbeth A. van Liere,[1] Ruixue Yuan,[1] Richard Wubbolts,[1] Alain de Bruin,[1,3] and Bart Westendorp[1,5,*]

[1]Department of Biomolecular Health Sciences, Faculty of Veterinary Medicine, Utrecht University, Utrecht, the Netherlands
[2]Department of Clinical Sciences, Faculty of Veterinary Medicine, Utrecht University, Utrecht, the Netherlands
[3]Department of Pediatrics, University of Groningen, University Medical Center Groningen, Groningen, the Netherlands
[4]Present address: Hubrecht Institute-KNAW, Utrecht, the Netherlands
[5]Lead Contact
*Correspondence: b.westendorp@uu.nl
https://doi.org/10.1016/j.celrep.2020.108449

SUMMARY

E2F transcription factors control the expression of cell-cycle genes. Cancers often demonstrate enhanced E2F target gene expression, which can be explained by increased percentages of replicating cells. However, we demonstrate in human cancer biopsy specimens that individual neoplastic cells display abnormally high levels of E2F-dependent transcription. To mimic this situation, we delete the atypical E2F repressors (E2F7/8) or overexpress the E2F3 activator in untransformed cells. Cells with elevated E2F activity during S/G2 phase fail to exit the cell cycle after DNA damage and undergo mitosis. In contrast, wild-type cells complete S phase and then exit the cell cycle by activating the APC/C^{Cdh1} via repression of the E2F target Emi1. Many arrested wild-type cells eventually inactivate APC/C^{Cdh1} to execute a second round of DNA replication and mitosis, thereby becoming tetraploid. Cells with elevated E2F transcription fail to exit the cell cycle after DNA damage, which potentially causes genomic instability, promotes malignant progression, and reduces drug sensitivity.

INTRODUCTION

The decision to commit to a new round of S phase is a pivotal step in the cell cycle. This step is irreversibly enforced by activation of E2F transcription factors and inactivation of the anaphase-promoting complex/cyclosome (APC/C) E3 ligase complex (Cappell et al., 2016). Activator E2F transcription factors (E2F1–E2F3) induce expression of a large network of genes. These E2F target genes include genes involved in S-phase entry and progression and cyclin E and Emi1, which inactivate the APC/C^{Cdh1} to allow rapid accumulation of proteins that are essential for S-phase progression. As S phase proceeds, E2F-dependent transcription is silenced again, which is then mediated by atypical repressor E2Fs (E2F7/8) (Bertoli et al., 2013; Kent and Leone, 2019).

It is widely recognized that E2F-dependent transcription is almost always increased in neoplastic versus normal tissues. In fact, high expression of this transcription program correlates strongly with poor prognosis in various types of cancer (Kent et al., 2016; Lan et al., 2018). However, it is to date unclear if the increase in E2F-target gene expression in cancer is only simply explained by the fact that the number of cycling cells in a neoplasm is increased or if individual cells have also increased E2F-target gene expression. In cells that already have entered S phase, heterogeneity in E2F-dependent transcription may have profound effects on cell-cycle fates, especially under conditions causing replication stress and DNA damage, since E2F targets include DNA replication and repair genes (Bertoli et al., 2016). Cells are vulnerable to DNA damage during S phase, and under conditions of genotoxic stress, cells must decide either to repair the damage and proceed to undergo mitosis or to arrest and exit the cell cycle (Gire and Dulic, 2015). The machinery underlying this decision point must also show switch-like behavior, because the decision to either arrest or continue the cell cycle is binary. However, in contrast to the G1/S transition, the pathways underlying the switch-like behavior of cells enforcing a cell-cycle arrest are far less well studied.

We propose that the combined action of factors controlling E2F-dependent transcription once the cell cycle is ongoing determines the decision to stop or continue cycling during genotoxic stress. These factors include expression of activator and repressor E2Fs, cyclin-dependent kinases (CDKs), ubiquitin ligases, and CDK inhibitors, many of which can be disturbed in cancer cells.

Here, we show that E2F-dependent transcription is elevated at single-cell level in cycling cancer cells from human biopsies. Furthermore, we found that deregulation of E2F-dependent transcription during S/G2 phase in non-transformed cells has profound consequences on cell-cycle fate in response to DNA damage. We observed that constrained E2F-dependent transcription

is of critical importance to initiate a long-term arrest of G2 cells after genotoxic stress. We characterized this arrest as a 4N-G1 state, because a large subset of arrested cells could re-enter the cell cycle to undergo another round of S phase and subsequent mitosis, leading to tetraploidy. In contrast, S-phase cells either overexpressing the E2F3 activator or lacking E2F7/8 repressors failed to suppress the E2F-target Emi1, which inhibits the APC/C^{Cdh1}, and progressed to undergo unscheduled mitosis. Finally, we demonstrate that E2F7/8 repressors cooperate with P53 and its target gene, P21, to enforce the 4N-G1 arrest. Hence, the combined action of multiple mechanisms affecting expression of E2F target genes (in particular Emi1) underlies the switch-like decision of cells to arrest in G2 or proceed to mitosis. This decision is pivotal to control genomic integrity in human cells.

RESULTS

Abnormally High E2F-Dependent Transcription in Individual Cancer Cells in Human Biopsy Specimens

We leveraged publicly available single-cell RNA sequencing data to determine if E2F-dependent transcription is elevated in cancer at the single-cell level. First, we analyzed a dataset containing almost 6,000 cells from 18 head and neck squamous cell carcinoma (HNSCC) patients (Puram et al., 2017). Although E2F-dependent transcription is deregulated at the bulk sample level in many cancers, HNSCC is of particular interest. Loss of repressor E2Fs drives malignant progression of keratinocytes (Thurlings et al., 2017). Furthermore, enhanced E2F-dependent transcription caused by nuclear export of the E2F7 repressor drives chemotherapy resistance in HNSCC patients (Saenz-Ponce et al., 2018). As a proxy for overall E2F transcription, we computed for each cell the average *Z* scores of a set of 80 different E2F target genes (Figure 1A). We had previously verified these 80 genes as E2F targets using chromatin immunoprecipitation (ChIP) sequencing, motif analysis, and microarrays (Westendorp et al., 2012). Dimensionality reduction using t-distributed stochastic neighbor embedding (tSNE) revealed well-separated clusters of different stromal cell types and three main clusters of malignant cells (Figure 1B, upper panel). The three tumor cell clusters clearly contained more cells with high E2F scores when we projected these scores on the tSNE maps (Figure 1B, lower panel). Boxplots also demonstrated that E2F scores were clearly elevated in HNSCC cells versus all non-tumor cells (Figure 1C). Plotting RNA counts of individual E2F target genes consistently showed the same pattern (Figure S1A), suggesting that indeed single cancer cells exhibit enhanced E2F-dependent transcription. Importantly, this could not simply be explained by overall elevated mRNA levels, as ubiquitously expressed genes and mesenchyme-specific genes showed completely different expression distributions (Figure S1A).

A limitation of this dataset is that HNSCC cells could not directly be compared to their non-transformed counterparts (i.e., normal epithelium). We could only compare tumor to various stromal cell types. Ideally, we would want to compare E2F-dependent transcription in cycling cancer and normal cells within the same tissue type. Currently, the only large dataset suitable to do such analysis is available from a recent study on acute myeloid leukemia (AML) patients (van Galen et al., 2019). AML is a rapidly proliferating cancer, but several normal cell types in the blood proliferate rapidly as well. Thus, we can compare E2F scores in cancer cells with adequate numbers of cycling non-malignant cells. First, we confirmed that E2F scores were overall strongly elevated in neoplastic cells versus non-transformed cell types in almost every individual patient, without taking into consideration the specific cell type (Figures 1E and S1B). We then compared the E2F scores between specific normal white blood cell types and their malignant counterparts in cycling and non-cycling cells separately. Although heterogeneity was substantial, malignant cell types clustered relatively well together with their non-malignant counterparts, confirming overall resemblance in gene expression (Figures S2A and S2B).

When comparing malignant cell types to their non-transformed counterparts, we observed that E2F scores were elevated in cancer cells. In particular malignant cells resembling conventional dendritic cells (cDCs), granulocyte-macrophage progenitors (GMPs), promonocytes (ProMonos), and progenitors (Progs) showed a statistically significant enhancement of E2F-dependent transcription compared to their non-transformed cycling counterparts (Figure 1F).

Together, these data strongly suggest that E2F-dependent transcription is highly heterogeneous between different types of cycling cells and, in particular, is elevated in cancer cells. As E2F-target genes include genes involved in DNA repair and cell-cycle progression, variation can have profound effects on cell-cycle fates, beyond overriding the G1/S checkpoint. However, it is challenging to study this further in patient-derived material, because cell-cycle stage could only be inferred from transcriptomic information. Furthermore, it is impossible to dissect the direct consequences of E2F de-repression during S/G2 phase and the indirect effects of overriding the G1/S checkpoint from these patient samples. Therefore, we decided to analyze the effects of unrestrained E2F-dependent transcription on DNA damage responses at single-cell level in a more controlled setting (i.e., in cells expressing high levels of E2F transcription during S and G2 phase). To this end, we used RPE cells carrying the fluorescent ubiquitination-based cell cycle indicator (FUCCI) reporter system in which we had deleted E2F7 and E2F8 using CRISPR-Cas9. We made double mutants (hereafter referred to as *E2F7/8*^{KO} cells), because substantial functional redundancy exists between these two highly homologous family members (Li et al., 2008; Thurlings et al., 2017).

Deregulated E2F-Dependent Transcription during S/G2 Phase Causes Cell-Cycle Fate Defects

Since E2F7/8 are only present during the S/G2 phase of the cell cycle (Boekhout et al., 2016), we first wanted to establish that *E2F7/8*^{KO} cells specifically show target gene deregulation during these phases. The FUCCI system allows to distinguish G1 cells from S and G2 cells via the alternating degradation of Azami green (mAG)-tagged truncated geminin and degradation of Kusabira orange (mKO)-tagged truncated CDT1 (Sakaue-Sawano et al., 2008). Therefore, we sorted cells according to expression levels of the FUCCI reporters and then quantified the expression of multiple E2F target genes in control and *E2F7/8*^{KO} cells. We observed that E2F7/8 loss only enhanced the expression of

CellPress
OPEN ACCESS

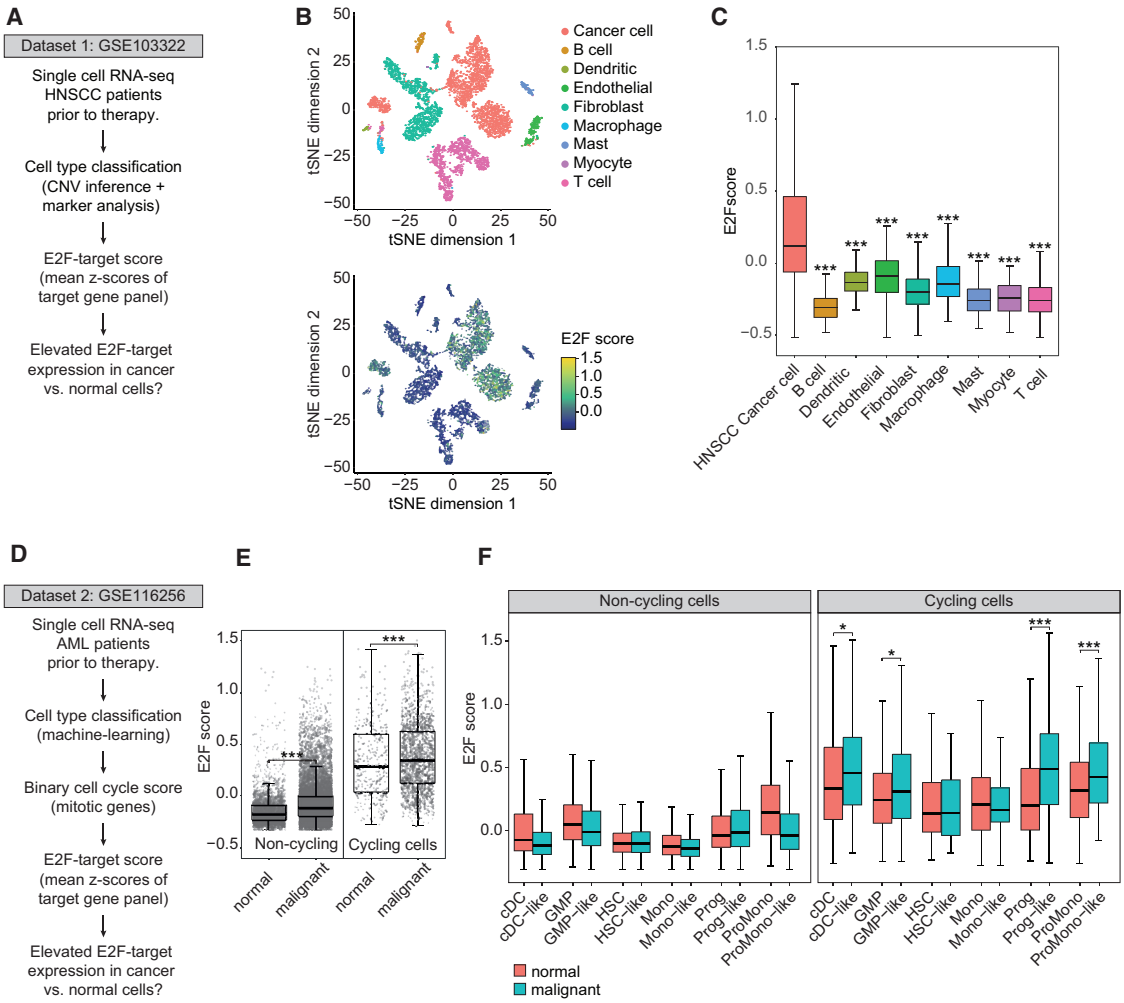

Figure 1. Elevated E2F-Dependent Transcription in Malignant versus Non-transformed Single Cells

(A) Schematic overview of the workflow to analyze E2F-target gene expression in single cells from patients with head and neck squamous cell carcinoma (HNSCC).

(B) Dimensionality reduction using t-stochastic neighborhood embedding (tSNE) shows clusters of HNSCC tumor cells and different types of stromal cells.

(C) Boxplots representing E2F-target expression scores of HNSCC tumor cells and different stromal cell types. ***$p < 0.0001$ as indicated, Kruskal-Wallis test followed by Dunnett's pairwise comparisons with post hoc Benjamini-Hochberg correction.

(D) Schematic overview of the workflow to analyze E2F-target gene expression in single cells from patients with acute myeloid leukemia (AML).

(E) E2F-target gene expression scores in malignant versus non-malignant cells from AML patients. The two panels respectively show cycling and non-cycling cells according to binary scores determined in the original publication (van Galen et al., 2019).

(F) Boxplots representing E2F-target expression scores of malignant cells from AML patients versus non-malignant cells from AML patients as well as healthy donors, grouped according to cell-type classification. cDC, conventional dendritic cell; GMP, granulocyte-macrophage progenitor; HSC, hematopoietic stem cell; Mono, monocyte; Prog, progenitor; ProMono, promonocyte. The addition "-like" refers to the best matching normal cell-type identity in malignant cells. *$p < 0.05$, ***$p < 0.005$ as indicated, Wilcoxon paired-rank tests with post hoc Benjamini-Hochberg correction.

target genes when cells were in S or G2 phase (Figure 2A). This suggests that *E2F7/8*^{KO} cells still have an intact G1/S checkpoint. In fact, live-cell imaging showed that *E2F7/8*^{KO} G1 cells were less likely to enter S phase under unperturbed conditions than control cells (Figures 2B and S3A). This was also reflected by lower proliferation rates during unperturbed conditions (Figure S3B).

These observations could be explained by the notion that E2F deregulation in the *E2F7/8*^{KO} cells causes mild replication-stress-induced DNA damage, which cannot be completely resolved prior to mitosis. To test this hypothesis, we transduced the FUCCI-expressing cells with mTurquoise-tagged truncated 53BP1. Despite the absence of the replication stress marker pCHK1-S345 in *E2F7/8*^{KO} cells (Figure S3C), we observed a small but significant increase in 53BP1 foci in Gem^{pos} (S/G2 phase) cells, suggestive of mild replication stress (Figure S3D). Unresolved endogenous replication stress in the mother cells can cause daughter cells to enter quiescence (Arora et al.,

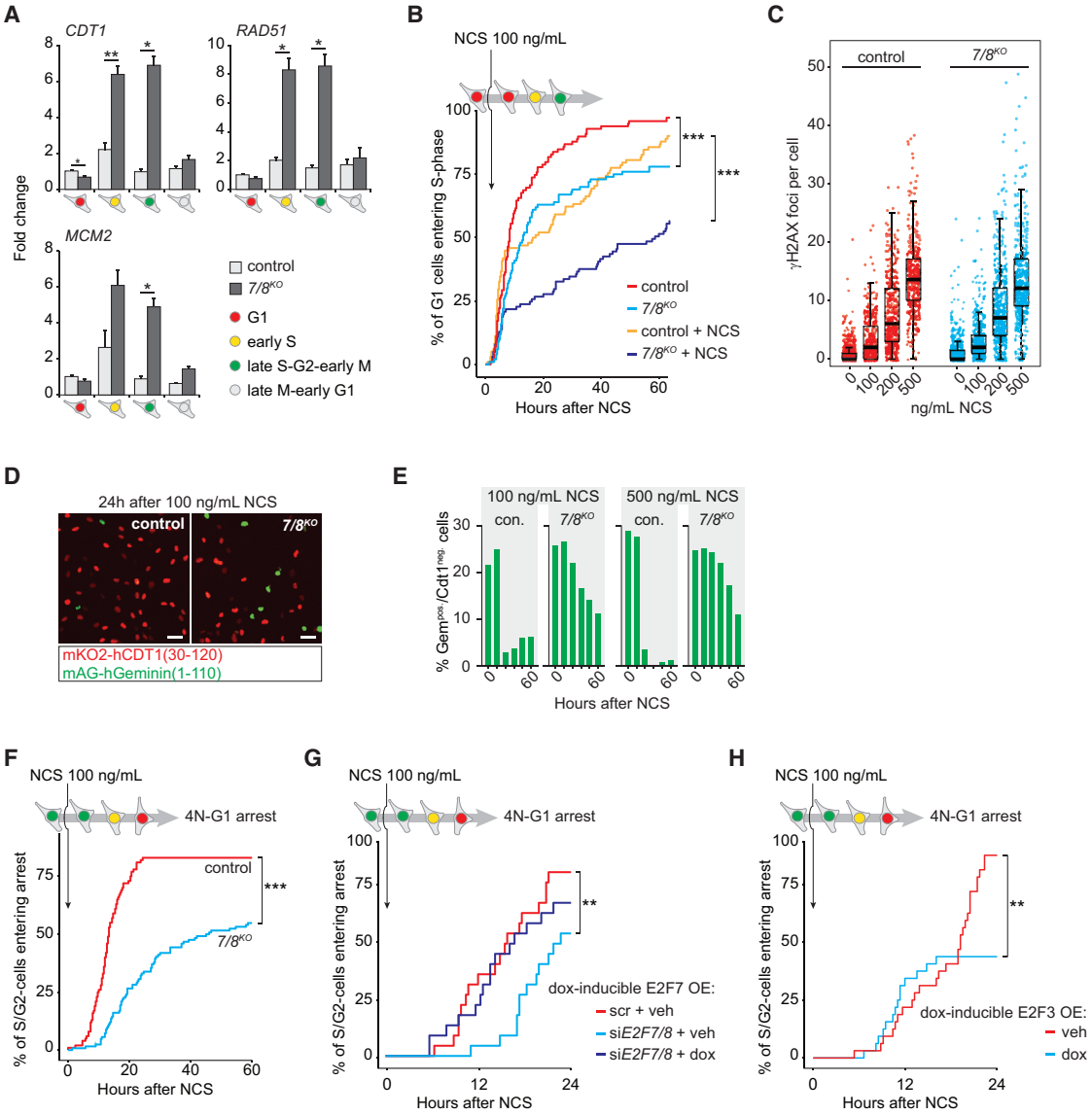

Figure 2. Deregulated E2F-Target Gene Expression during S/G2 Phase Results in Aberrant DNA Damage Response

(A) qPCR on FACS-sorted FUCCI-expressing cells, showing cell-cycle-dependent deregulation of E2F target genes in *E2F7/8*^{KO} cells. Bar represents mean ± SEM from a total of three experiments.

(B) Time until S-phase entry in control and *E2F7/8*^{KO} RPE-FUCCI cells in unperturbed conditions or after addition of 100 ng/mL neocarzinostatin (NCS), quantified as cumulative entry of G1 cells into S phase during live-cell imaging. S-phase entry was determined by appearance of geminin. Data from two independent cell clones were pooled (n = 100 cells in total, 50 per clone).

(C) Quantification of γH2AX foci per cell 8 h after a single dose of NCS.

(D) Snapshot of RPE-FUCCI cells taken 24 h after treating cells with 100 ng/mL NCS. Scale bar represents 50 μm.

(E) Quantification of percentage Gem^{pos}/CDT1^{neg} cells after NCS treatment. In each condition, at least 500 cells were quantified.

(F) Cumulative numbers of cells re-activating the APC/C^{Cdh1} during G2 in response to NCS. Per-condition fates of 100 S/G2 cells from two independent control and *E2F7/8*^{KO} clones were determined during 60 h of live-cell imaging.

(G) Cumulative numbers of cells re-activating the APC/C^{Cdh1} in response to 100 ng/mL NCS after transfection with siE2F7/8 with or without doxycycline-inducible overexpression (OE) of mTurquoise-tagged murine E2F7. Per condition fates of 50 S/G2 cells were determined during 24 h of live-cell imaging. The siRNA was designed against human E2F7 and did not affect the overexpression construct.

(H) Same as in (G), but now using cells with doxycycline-inducible expression of E2F3 and without siRNA transfections.

2017). Indeed, live-cell imaging showed that a significantly increased percentage of *E2F7/8*^{KO} cells in G1 contained 53BP1 nuclear bodies, which correlated with a G1 arrest (Figure S3E). Together, these data show that loss of E2F repressors leads to a modest increase in replication stress under unperturbed conditions.

Next, we investigated if uncontrolled E2F-dependent transcription during S phase also results in an altered response to exogenous DNA damage. We treated cells with the radiomimetic drug neocarzinostatin (NCS), which causes double-stranded DNA breaks (DSBs) irrespective of cell-cycle phase (Chao et al., 2017). Furthermore, NCS is highly unstable, which allows cells to recover without the need to wash the drug away during live-cell imaging experiments. When treated with 100 ng/mL NCS, the *E2F7/8*^{KO} G1 cells were still significantly less likely to enter S phase than control cells during the imaging period (Figure 2B).

We then quantified DNA damage with immunofluorescence staining of γH2AX. NCS dose-dependently induced similar levels of DNA damage in control and *E2F7/8*^{KO} cells (Figure 2C). Although a low dose (100 ng/mL) of NCS only caused modest DNA damage, it was sufficient to strongly inhibit proliferation of both control and *E2F7/8*^{KO} cells over a period of 60 h of imaging (Figure S3B). Despite similar levels of DNA damage, *E2F7/8*^{KO} cells showed a strong increase in the percentage of geminin-positive/CDT1-negative (hereafter referred as Gem^{pos}/CDT1^{neg}) cells 1 and 3 days after NCS treatment, indicating an enhanced number of cycling cells despite DNA damage (Figures 2D and 2E). According to the expected cell-cycle-dependent degradation of the FUCCI reporters, these are cells in mid-to-late S phase or G2. Therefore, we followed the fates of cycling (i.e., Gem^{pos}/CDT1^{neg}) cells after addition of NCS. Indeed, we saw that within 24 h, the majority of control cells in S/G2 phase responded to NCS by exiting the cell cycle and entering a G1-like state, as seen by loss of geminin and reappearance of CDT1 without mitosis (Figure 2F; Video S1). Disappearance of the geminin-mAG signal is caused by activation of the APC/C^{Cdh1} complex. This complex is active during late mitosis and G1 but can also be re-activated in response to DNA damage to exit the ongoing cell cycle (Bassermann et al., 2008). This arrest was severely delayed in *E2F7/8*^{KO} cells (Figure 2F), explaining the elevated level of Gem^{pos}/CDT1^{neg} cells compared to control cells.

To bear out the hypothesis that balanced E2F-dependent transcription is essential to exit the cell cycle after DNA damage in S/G2, we created a doxycycline-inducible expression system for E2F3 and E2F7 in RPE cells carrying the FUCCI4 system (Bajar et al., 2016). Similar to *E2F7/8*^{KO} cells, knockdown of E2F7/8 prevented APC/C^{Cdh1} activation after DNA damage (Figure 2G), but overexpression of E2F7 inhibited expression of E2F target genes and re-enabled cell-cycle exit (Figures 2G and S3F). Moreover, overexpression of the activating transcription factor E2F3 mimics the phenotype observed in *E2F7/8*^{KO} cells (Figures 2H and S3G), confirming that any disbalance in E2F-dependent transcription during S/G2 phase perturbs cell-cycle exit after DNA damage.

DNA Damage in S or G2 Phase Leads to a Cell-Cycle Exit in G2

We then asked if the re-activation of the APC/C^{Cdh1} already happened during S phase or whether cells first completed S phase to arrest in G2 in response to NCS. To answer this question, we analyzed their DNA content with flow cytometry. This showed that 8 h after addition of NCS, virtually all Gem^{pos}/CDT1^{neg} cells had a 4N DNA content (Figure 3A). 24 h after NCS treatment, a substantial 4N-Gem^{neg} cell population had appeared (Figure 3B). These cells were not arrested in mitosis, because pH3^{pos}-Gem^{neg} cells were absent 24 h after NCS treatment (Figure S3H). Abortive mitosis did also not explain the appearance of Gem^{neg}-4N cells, because the percentage of binucleated cells was not increased (Figure S3I). This suggests that cells finish S phase before entering the G1-like state. We will therefore refer to this cell-cycle exit as a 4N-G1 arrest. We then tested whether cell-cycle exit was restricted to cells in S phase at the moment of DSB induction or whether G2 cells could also undergo this fate. To this end, we pulsed cells with the thymidine analogue EdU and simultaneously added NCS. We found EdU-positive as well as EdU-negative 4N-Gem^{neg} cells 24 h after NCS treatment, demonstrating that both S- and G2-phase cells encountering DNA damage can exit the cell cycle by activating APC/C^{Cdh1} (Figure 3C). Similarly, *E2F7/8*^{KO} cells presented an EdU-positive and EdU-negative 4N cell population (Figure 3C). However, these populations were predominantly Gem^{pos}, confirming that both S- and G2-phase cells lacking E2F7/8 have a reduced capacity to activate the APC/C^{Cdh1} and exit the cell cycle.

Further cell fate analysis of Gem^{pos}/CDT1^{neg} cells showed that more than twice as many Gem^{pos}/CDT1^{neg} *E2F7/8*^{KO} as control cells did not arrest in response to 100 ng/mL NCS and proceeded to unscheduled mitosis (Figure 3D). This unscheduled mitosis in *E2F7/8*^{KO} cells resulted in daughter cells containing 53BP1 nuclear bodies, which mostly remained in G1, indicating unresolved DNA damage in these *E2F7/8*^{KO} cells (Figures 3E and S3J). When we activated the DNA checkpoint with a high dose of NCS (200 ng/mL), nearly all S- and G2-phase cells responded by either arresting in G2 phase or entering a G1-like arrest (Figures 3F and 3G). Interestingly, inhibition of the G2/M checkpoint by the WEE1 inhibitor adavosertib greatly increased the population of both control and *E2F7/8*^{KO} cells proceeding to mitosis after NCS treatment, showing a dependency on the G2/M checkpoint to ensure cell-cycle arrest, irrespective of APC/C^{Cdh1} activation (Figures 3F and 3G). Together, these results show that cells in S and G2 phase respond to DSBs with a 4N-G1-like arrest in an E2F7/8-dependent manner.

The G1-like State in NCS-Treated Cells Is Transcriptionally Enforced by E2F7/8

Hitherto, we defined the G1-like state by only the loss of geminin and appearance of CDT1. To gain further insight into this biological state, we performed single-cell RNA sequencing on control and *E2F7/8*^{KO} cells 24 and 48 h after treatment with NCS. To this end, we used an automated RNA-sequencing platform (Muraro et al., 2016). However, instead of capturing the cells with fluorescence-activated cell sorting (FACS), we isolated and captured cells with a VyCAP needle puncher (Figure 4A). This system is designed to take fluorescence images of up to 6,400 individual cells, from which cells of interest can be automatically selected and isolated for single-cell genomics and transcriptomics (Stevens et al., 2018). Using an ultrafine needle mounted to a motorized z-stage, cells are punched from the chip into a microwell plate (Figure 4B). This procedure allowed us to perform RNA sequencing on cells with a known FUCCI fluorescence status. The fluorescence signals of the punched cells showed that all cell-cycle phases were captured from both the untreated control and *E2F7/8*^{KO} cell lines (Figure S4A). However, treatment with 200 ng/mL NCS showed a

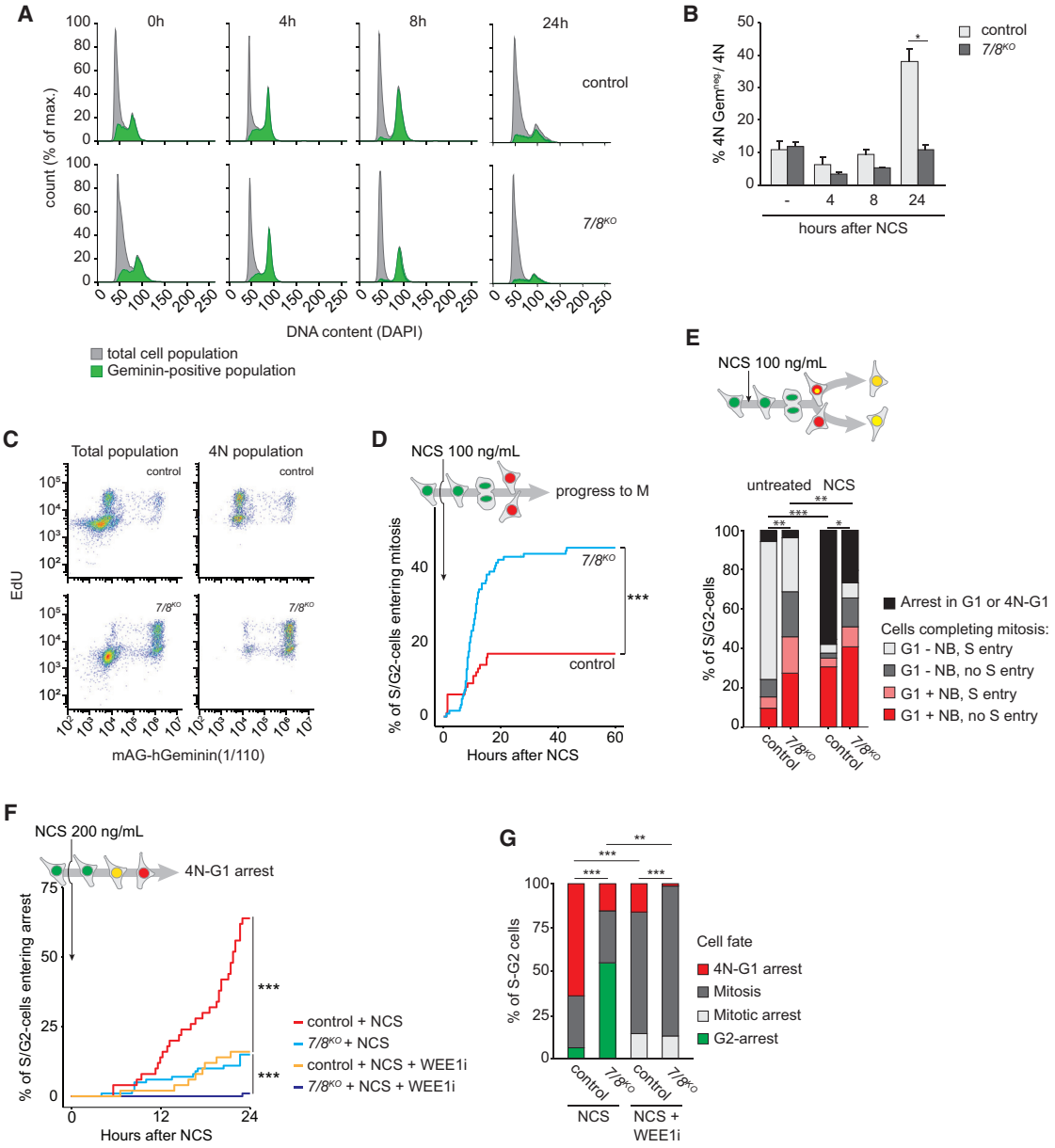

Figure 3. E2F7/8 Prevent Unscheduled Mitosis after DNA Damage

(A) Flow cytometry analysis of DNA content in RPE-FUCCI cells in response to 100 ng/mL NCS. Green histograms represent Gem^{pos} cells.

(B) Quantification of (A) showing 4N Gem^{pos} cells as percentage of the total 4N population. Bar represents mean ± SEM from a total of three experiments.

(C) Flow cytometric plot of control and *E2F7/8*^{KO} cells 24 h after simultaneous NCS treatment (200 ng/mL) and EdU pulse.

(D) Quantification of S/G2 cells that underwent mitosis after treatment with 100 ng/mL NCS, observed by live-cell imaging. Per condition, at least 100 cells from two different CRISPR clones were followed.

(E) Stacked bar graphs of fates of S/G2 cells in response to 100 ng/mL NCS, evaluated by live-cell imaging. NB, 53BP1 nuclear body. Per condition fates of 50 cells of two independent clones were analyzed.

(F) Cumulative frequency of S/G2 cells entering a G1-like arrest after simultaneous treatment with NCS (200 ng/mL) and the Wee1 inhibitor adavosertib (2.5 μM) analyzed by live-cell imaging. n = 50 cells of two clones per condition were analyzed.

(G) Stacked bar chart showing the quantification of different fates of S/G2 cells of the experiment described in (F). Per condition, n = 50 cells of two independent clones were analyzed.

marked increase in the number of quiescent or G1-like (Gem^{neg}/$CDT1^{pos}$) cells. At 24 h, we observed again a clear increase in the number of Gem^{pos}/$CDT1^{neg}$ cells when comparing *E2F7/8*^{KO} with control cells (Figure S4A). In total, 180 cells passed our rigorous quality control. By unsupervised clustering based on the 2,000 most variable genes, we could identify four main

CellPress
OPEN ACCESS

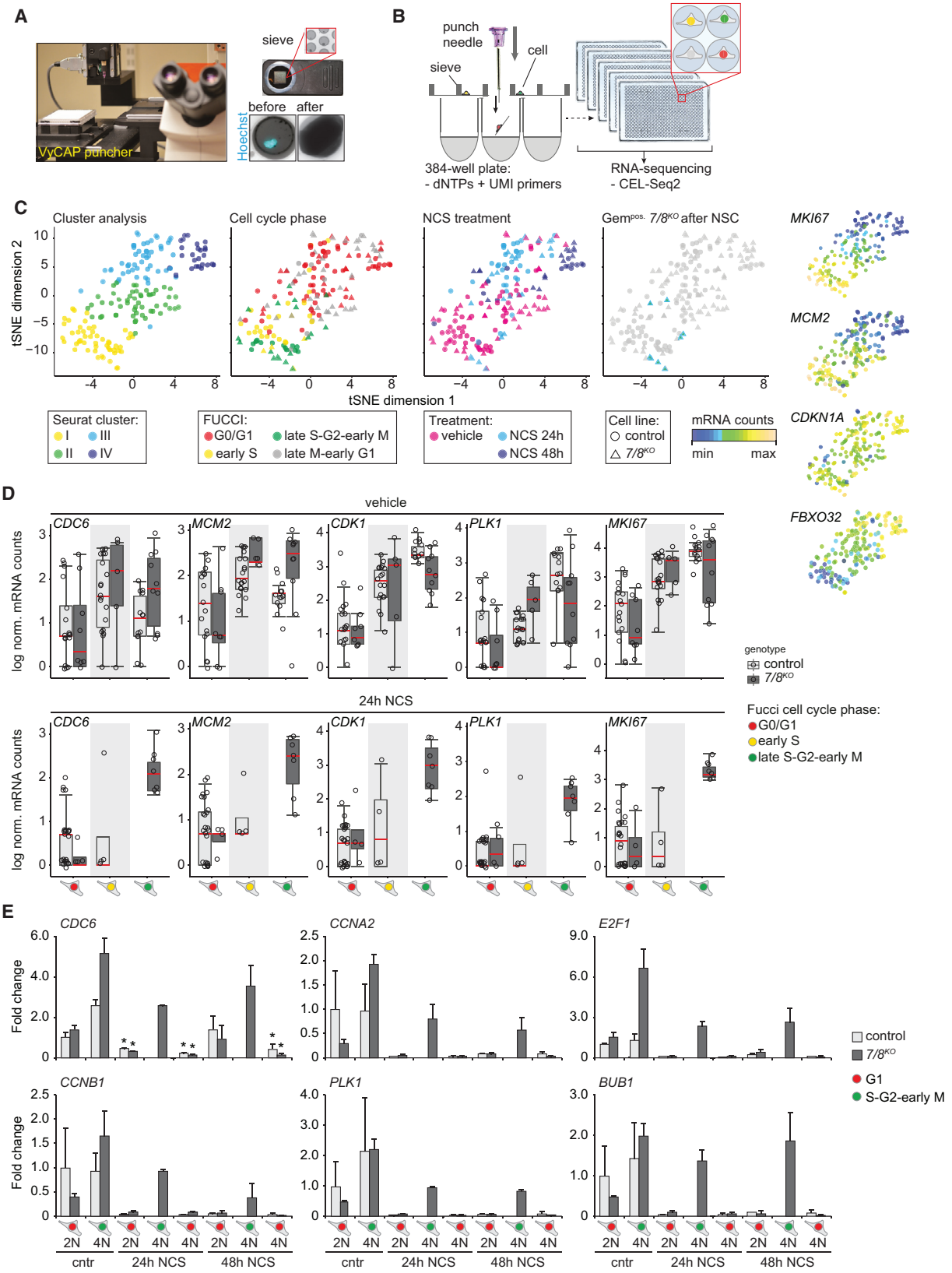

(legend on next page)

clusters of cells (Figure 4C). These clusters correlated well with cell-cycle phase and NCS treatment. Clusters I and II corresponded with untreated S/G2 cells and G1 cells, respectively. Clusters III and IV respectively consisted of arrested cells 24 and 48 h after NCS treatment (Figure 4C). The expression of cell-cycle genes such as *MKI67* and the E2F target gene *MCM2* showed the highest expression in cluster I, whereas stress-related genes, including the P21-encoding *CDKN1A* and *FBXO32*, were most highly expressed in cluster IV (48 h NCS). Thus, the observed 4N-G1 cell-cycle arrest upon NCS treatment coincides with a transcriptional state similar to G0/G1 cells. To further confirm this, we performed differential expression analysis on Gem^{neg} untreated and NCS-treated cells. The total cell numbers were low and hence we found only a handful of statistically significant NCS-induced expression alterations (Figure S4B). Notwithstanding these results, overall, single-cell gene expression of cell-cycle markers was decreased and P53 target genes were increased in Gem^{neg}/Cdt1^{pos} control cells after NCS treatment (Figure S4C).

Overall, the *E2F7/8^{KO}* cells and control cells were not separated by the cluster analysis, suggesting that expression profiles of non-cell-cycle genes were comparable (Figure 4C). Interestingly, we observed several strongly Gem^{pos} NCS-treated *E2F7/8^{KO}* cells in clusters I and II. These cells most likely represent the previously observed S/G2-phase cells which were unable to activate APC/C^{Cdh1} and did not arrest in a G1-like state in response to NCS. Clusters I and II largely contain untreated cycling cells, suggesting that E2F7/8 mutant cells failing to degrade geminin after NCS showed S/G2-like cell-cycle gene expression profiles. To further study this, we grouped the single-cell gene expression profiles of the *E2F7/8^{KO}* cells and control cells by cell-cycle status as determined by FUCCI reporters. Again, we observed upregulation of E2F target genes, including *CDC6* and *MCM2*, during S and G2 phase in untreated *E2F7/8^{KO}* cells (Figure 4D, upper row). In contrast, FOXM1 target genes, exemplified here by *CDK1* and *PLK1*, and the general cell-cycle marker MKI67 were not de-repressed in *E2F7/8^{KO}* cells during unperturbed G2 phase (Figure 4D, upper row). However, when examining expression of these genes after NCS treatment, expression of E2F target genes was strongly elevated in Gem^{pos}/CDT1$^{neg.}$ *E2F7/8^{KO}* cells 24 h after NCS treatment compared to Gem^{neg}/CDT1^{pos} cells of both genotypes (Figure 4D, bottom row). In addition, these cells showed strongly upregulated expression of mitotic B-Myb/FOXM1-target genes, including *CDK1* and *PLK1*, as well as *MKI67* (Figure 4D, bottom row). This indicates that the Gem^{pos} subset of *E2F7/8^{KO}* cells indeed remained in a S- or G2-like state. We did not observe these Gem^{pos}/CDT1^{neg} cells after 48 h, but we only managed to capture a low number of cells at this time point (Figure S4D).

In a parallel approach, we performed pseudo-time alignment using the Monocle algorithm (Trapnell et al., 2014). Monocle is a well-established tool that can use transcriptome data to order single cells according to their progression between different states, such as differentiation or cell-cycle phase. This pseudo-time alignment showed that in our single-cell dataset cells were indeed ordered according to expression changes in cell-cycle genes and genes related to cell stress (Figure S5A). Importantly, Monocle analysis confirmed in an unsupervised manner that Gem^{pos}/CDT1^{neg} *E2F7/8^{KO}* cells after NCS treatment maintained an S/G2-like expression profile (Figure S5A).

Our single-cell approach does not allow us to distinguish 2N-Gem^{neg}/CDT1^{pos} and 4N-Gem^{neg}/CDT1^{pos} cells. We therefore FACS-sorted 2N-Gem^{neg}/CDT1^{pos}, 4N-Gem^{neg}/CDT1^{pos}, and 4N-Gem^{pos}/CDT1^{neg} cells using a fluorescent cell-cycle dye for subsequent gene expression analysis (Figure S5B). To support our single-cell RNA-sequencing data, we first verified the expression of a small subset of significantly differentially expressed genes in NCS-treated versus control G1 (Cdt1^{pos}/Gem^{neg}) cells (Figure S5C). Next, we found that NCS treatment resulted in upregulation of several P53 targets in both 2N and 4N Gem^{neg} and Gem^{pos} cells compared to untreated cells (Figure S5D). Moreover, consistent with the single-cell expression data, cell-cycle and mitotic markers were virtually absent in NCS-treated 4N-Gem^{neg} cells and even lower expressed than in untreated G1 cells (Figure 4E). However, 4N-Gem^{pos} cells after NCS treatment, which were solely present in the *E2F7/8^{KO}* condition, failed to downregulate these cell-cycle genes (Figure 4E). Together, these single-cell RNA-sequencing and FACS-qPCR data show that the DNA-damage-induced 4N-G1 arrest indeed resembles a G1-like gene expression profile and that atypical E2Fs are of pivotal importance to enforce these transcriptomic changes.

Repression of the E2F7/8 Target Gene FBXO5 Is Required to Mediate the 4N-G1 Arrest in Response to DNA Damage

Because atypical E2Fs are transcriptional repressors, we asked downregulation of which target genes are critical to enter a G1-like state after DNA damage. The G1-like state is established by re-activation of APC/C^{Cdh1}, as exemplified by APC/C dependent degradation of the FUCCI reporter geminin. A key candidate effector would be *FBXO5*, which encodes the endogenous APC/C^{Cdh1} inhibitor Emi1. Previous work showed that P53-dependent activation of P21 can activate APC/C^{Cdh1} via repression of Emi1 expression in arrested G2 cells after genotoxic

Figure 4. Single-Cell Transcriptomics Reveal Deregulation of E2F Transcription as well as the Mitotic (B-Myb/FOXM1) Gene Expression Program after E2F7/8 Deletion

(A) VyCAP needle puncher system for capturing, imaging, and selection of cells for single-cell sequencing.

(B) Cartoon showing how the needle puncher is used to collect single cells in microwell plates for RNA sequencing.

(C) tSNE plots of single-cell mRNA sequencing on control and *E2F7/8^{KO}* cells with and without NCS treatment (200 ng/mL).

(D) mRNA counts of representative E2F targets (*CDC6* and *MCM2*) and FOXM1 targets (*CDK1* and *PLK1*) and the general cell-cycle marker *MKI67* from the single-cell sequencing data, separated by treatment, cell cycle, and genotype condition. The boxes indicate 25th, 50th, and 75th percentiles, and whiskers indicate 5th and 95th percentiles. Each condition represents at least four different cells.

(E) qPCR on NCS (200 ng/mL) treated cells FACS-sorted based on FUCCI markers and DNA content. Expression of representative cell-cycle (upper panel) and mitotic (lower panel) genes is shown. Bar represents mean ± SEM of two independent clones, both measured in duplicate. * $P < 0.05$ versus 2N untreated control cells.

CellPress
OPEN ACCESS

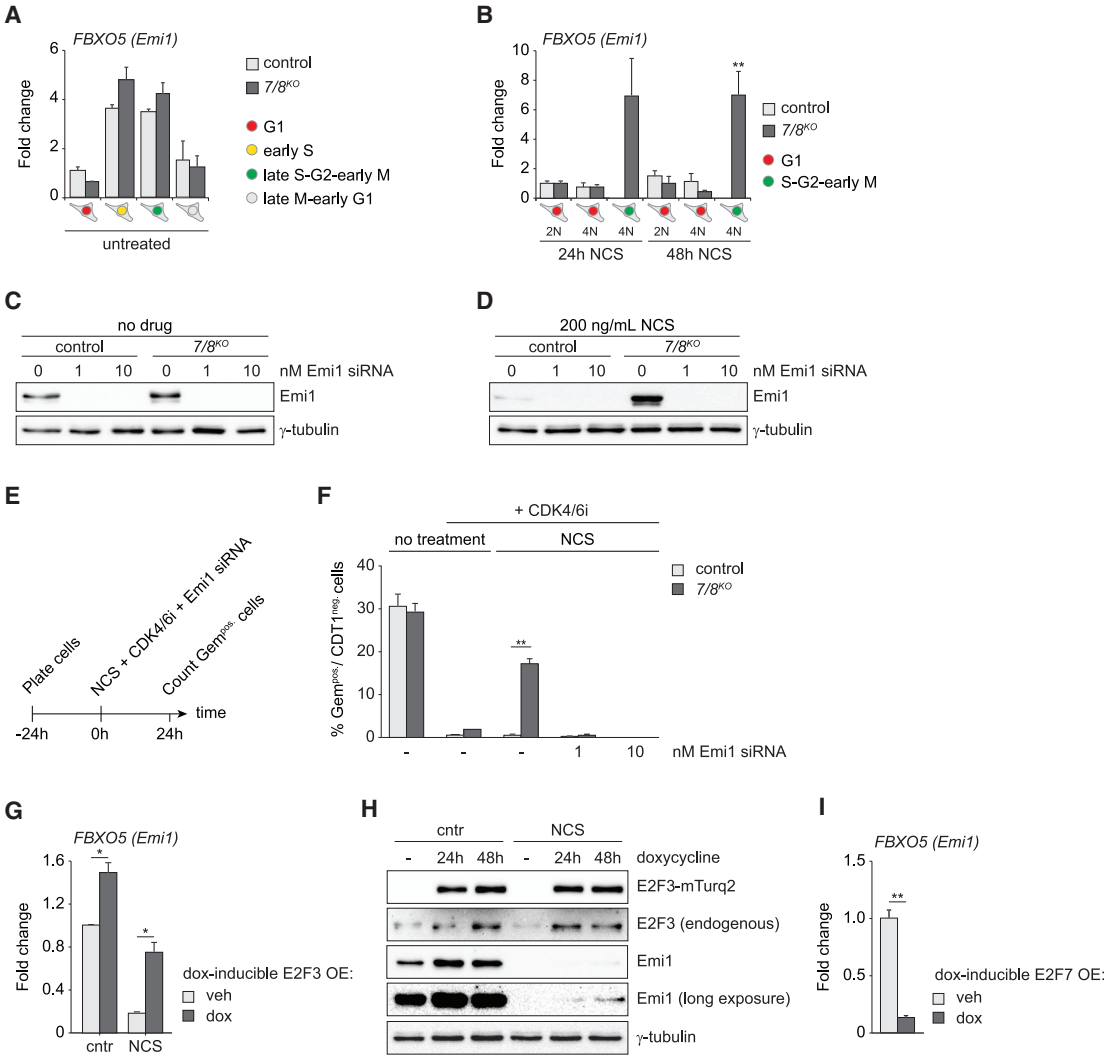

Figure 5. Failure of *E2F7/8^{KO}* Cells to Enter a G1-like Arrest after S Phase Is Caused by Upregulation of Emi1 Expression

(A) qPCR of *FBXO5* (Emi1) transcripts in FACS-sorted FUCCI-expressing cells in unperturbed *E2F7/8^{KO}* and control cells. Bar represents mean ± SEM from a total of three experiments.

(B) Same as (A), but 24 h and 48 h after 200 ng/mL NCS treatment.

(C) Immunoblot showing expression of Emi1 in unperturbed RPE-FUCCI cells and 24 h after addition of siRNA against Emi1. Blots are representative examples of two independent experiments.

(D) Same as in (C), but now in the presence of NCS.

(E) Experimental design of Emi1 siRNA transfections to rescue the capacity of *E2F7/8^{KO}* cells to enter a 4N-G1 arrest after NCS treatment. CDK4/6 inhibition prevented any G1 cells from entering S phase after NCS.

(F) Knockdown of *FBXO5* immediately after NCS treatment rescues the G1-like arrest in *E2F7/8^{KO}* cells. The percentage of Gem^{pos}/CDT1^{neg} cells was counted from fluorescence microscopy snapshots of living cells 24 h after 200 ng/mL NCS treatment. Bars represent the average ± SEM from a total of two experiments (two clones of cells in each experiment, n = 500 cells per condition). Differences in percentages of cells per condition were statistically evaluated using Fisher's exact tests.

(G) qPCR of *FBXO5* after 24 h of overexpression of E2F3 in the presence or absence of NCS (200 ng/mL). Bars represent the average ± SEM from a total of two experiments. OE, overexpression.

(H) Immunoblot showing elevated levels of Emi1 upon 24 or 48 h E2F3 overexpression in the presence or absence of NCS. Note elevated levels of endogenous E2F3 upon induction of exogenous E2F3, as E2F3 is an E2F target itself.

(I) qPCR of *FBXO5* after 24 h of overexpression of E2F7. Bars represent the average ± SEM of in total two experiments. OE, overexpression.

stress (Lee et al., 2009; Wiebusch and Hagemeier, 2010). We previously demonstrated that Emi1 is transcriptionally regulated by E2F7 and E2F8 (Boekhout et al., 2016). *FBXO5* transcripts were only modestly increased by E2F7/8 deletion in the FACS-sorted unperturbed FUCCI cells (Figure 5A). However, qPCR data showed that FBXO5 transcripts were highly elevated in the 4N-Gem^{pos}/CDT1^{neg} cells lacking E2F7/8 after NCS compared to NCS-treated 4N-G1 cells (Figure 5B).

Immunoblotting confirmed that Emi1 was strongly increased in NCS-treated *E2F7/8*^{KO} cells compared to control cells (Figures 5C and 5D).

If *E2F7/8*^{KO} cells fail to undergo a 4N-G1 arrest due to derepression of Emi1, then knockdown of Emi1 would rescue this defect. To test this, we used RNAi immediately after NCS addition to rescue the elevated expression of *FBXO5* (Emi1) in *E2F7/8*^{KO} cells and then counted the presence of Gem^{pos} cells after 24 h (Figure 5E). We treated the cells with a CDK4/6 inhibitor to prevent any G1 cells from entering S phase after the addition of NCS, and contributing to the Gem^{pos} cell population. Interestingly, a low dose of 1 nM Emi1 small interfering RNA (siRNA) was already sufficient to abolish the Emi1 overexpression and completely rescued the percentage of Gem^{pos}/CDT1^{neg} *E2F7/8*^{KO} cells to a level comparable to control cells (Figures 5D and 5F).

Alternative E2F effectors could be cyclin E1 and A2, which activate CDK2 and directly inhibit APC/C by phosphorylation of Cdh1 (Lukas et al., 1999). As CDKs are functionally redundant, we repeated the knockdown experiment but now with CDK1 and CDK2 RNAi (Figure S6A). Despite efficient knockdown, we observed no effect on the percentage of Gem^{pos} cells after NCS treatment (Figures S6B and S6C). Most likely, CDK is already inactivated by WEE1 after NCS treatment, explaining why siRNA did not have an additional effect.

In line with our earlier observations that inducible overexpression of the E2F activator E2F3 prevents cells from entering 4N-G1 similar to *E2F7/8*^{KO} cells, we found that Emi1 levels were elevated in E2F3-overexpressing cells after NCS treatment (Figures 5G and 5H). Finally, overexpression of E2F7, which could rescue the phenotype of cells depleted for E2F7/8, dramatically reduces the transcript levels of *FBXO5* (Figure 5I). Together, these data show that the balance in transcriptional control of Emi1 by E2F activators and repressors critically affects the decision to undergo a 4N-G1 arrest after DNA damage.

P53 and its target, P21, are also pivotal in downregulation of Emi1 to maintain a cell-cycle arrest in G2 after DNA damage (Lee et al., 2009; Wiebusch and Hagemeier, 2010). Other work showed that E2F7 is a direct transcriptional target gene of P53 (Aksoy et al., 2012; Carvajal et al., 2012). This raised the question to what extent E2F7/8 act in parallel with or downstream of P53 in this response. To this end, we knocked down *TP53* using siRNA and again quantified APC/C^{Cdh1} activation (Figure S7A). Knockdown of *TP53* resulted in strongly attenuated expression of its downstream target P21 after NCS treatment (Figures S7B and 6A). We observed that *TP53* knockdown caused a marked increase in Gem^{pos} cells after NCS treatment (Figure S7C). To exclude the possibility that knockdown of TP53 abrogates the G1/S checkpoint and that this contributes to the increase in Gem^{pos} cells, we co-treated cells with a CDK4/6 inhibitor (Figure 6B). Interestingly, the combination of E2F7/8 deletion and P53 knockdown caused a stronger increase in Gem^{pos} cells than either intervention alone after 48 h (Figure 6C). This suggests that E2F7/8 and P53 act in parallel pathways to establish activation of APC/C^{Cdh1} after DNA damage. In line with these observations, we found that E2F target genes in NCS-treated cells were upregulated by *TP53* RNAi, in particular in combination with E2F7/8 deletion (Figure 6D). Importantly, these upregulated target genes included the aforementioned APC/C^{Cdh1} inhibitor Emi1.

Previous work suggests that P21-dependent retinoblastoma (RB) dephosphorylation could at least in part explain the reduced Emi1 expression to enforce the cell-cycle arrest in G2 cells (Lee et al., 2009). Hence, we wanted to directly compare the importance of canonical repression via RB with the importance of atypical E2Fs on E2F target gene regulation and the initiation of a 4N-G1 arrest after DNA damage. To test this, we knocked down *RB1* in the same experimental setting as *TP53* (Figure S7A). Although RB1 protein and transcripts were nearly absent after siRNA treatment, we did not find a significant effect on the percentage of Gem^{pos} cells after NCS (Figure S7C–S7E). In line with this, *RB1* knockdown caused only a minor increase in E2F target gene expression (Figure S7F). These findings suggest that RB1 does not play an important role in mediating the 4N-G1 arrest. It is possible that other pocket proteins (P107 and P130) act redundantly with RB to sustain repression of E2F target genes under DNA-damaging conditions (Helmbold et al., 2009).

Together, these results strongly suggest that the combined action of atypical repressor E2Fs and P53 during S and G2 phase regulates expression of E2F target genes, in particular Emi1, to mediate APC/C^{Cdh1} re-activation and subsequent arrest of cycling cells in response to DNA damage independently of RB1.

Atypical E2Fs Mediate DNA-Damage-Induced Endocycles

We referred to the NCS-induced cell-cycle exit as a 4N-G1 arrest, but G1 implicates that these cells could escape the arrest and start a new round of S phase. Indeed, live-cell imaging revealed that a remarkably high percentage of NCS-treated S/G2 cells (~30%) could re-enter the cell cycle and complete mitosis after initially undergoing a 4N-G1 arrest (Figures 7A and 7B). However, cell-cycle reentry was virtually absent in *E2F7/8*^{KO} cells (Figure 7B). Accordingly, flow cytometry analysis showed the appearance of a substantial population of cycling (i.e., Gem^{pos}) cells with a 4–8N DNA content 3–6 days after NCS treatment in control RPE cells, but not in *E2F7/8*^{KO} cells (Figures 7C and 7D). This polyploidization phenomenon also led to gross mitosis defects, such as tripolar spindles (Figure 7E). Although *E2F7/8*^{KO} cells reentering the cell cycle are extremely rare, a direct role for atypical E2Fs in escape from the 4N-G1 like state is highly unlikely, as exogenous E2F7 is efficiently degraded by APC/C^{Cdh1} (Figures 7F and 7G). This coincides with the disappearance of geminin-mClover, which is efficiently degraded once the cells have entered the 4N-G1 arrest. Collectively these data demonstrate that cycling cells treated with a DNA-damaging drug can escape a 4N-G1 arrest, which can eventually lead to tetraploidy and aneuploidy. Atypical repressor E2Fs are critically important in initiating this route to polyploidy.

DISCUSSION

High levels of E2F-dependent transcription are seen in most cancers and correlate with poor prognosis. This can be explained by the fact that it corresponds with increased numbers of cycling

CellPress
OPEN ACCESS

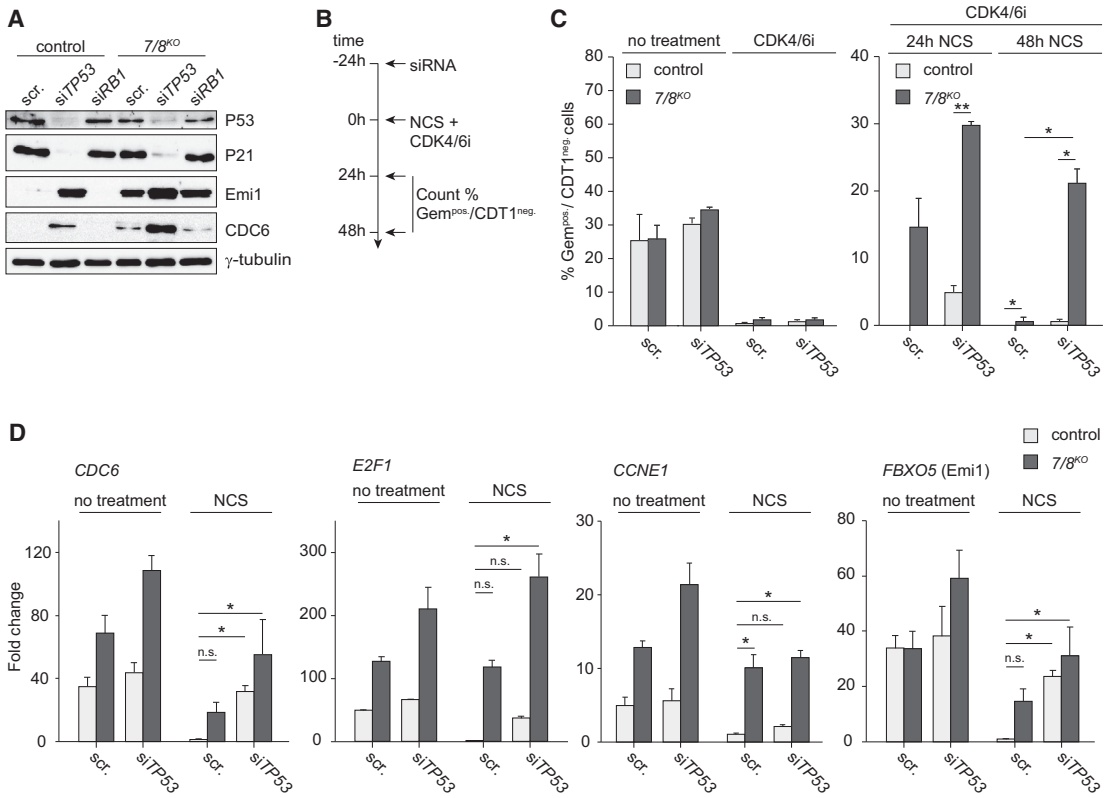

Figure 6. E2F7/8 and P53 Cooperate to Enforce a 4N-G1 Arrest after DNA Damage

(A) Immunoblot showing expression of indicated proteins in RPE-FUCCI cells 48 h after addition of P53 siRNA and 24 h after treatment with 500 ng/mL NCS. Blots are representative examples of two independent experiments.

(B) Experimental scheme of *TP53* siRNA knockdown experiments to study the interaction between E2F7/8 and P53 after NCS treatment. CDK4/6 inhibition prevented any G1 cells from entering S phase after NCS treatment.

(C) Quantification of the percentages of S/G2 (Gem^{pos}) cells 24 and 48 h after 500 ng/mL NCS treatment. Bars represent the average ± SEM from a total of two experiments (two clones of cells in each experiment). At least n = 500 cells per condition were counted. Differences in percentages of cells per condition were statistically evaluated using Fisher's exact tests.

(D) Effects of *TP53* knockdown and E2F7/8 deletion on E2F target genes in unperturbed conditions and 24 h after NCS treatment. Bars represent mean ± SEM of duplicate measurements in two independent cell clones.

cells. However, we now show that E2F-dependent transcription can also be abnormally high in single cycling cancer cells, which has a profound impact on their DNA damage responses and cell-cycle fate decision-making (Figure 7H).

Our mechanistic studies are largely in line with previous studies showing that P53 can arrest the cell cycle via activation of APC/C^{Cdh1} in response to genotoxic stress. The P53 target P21 inhibits Emi1, which would keep APC/C^{Cdh1} inactive until mitosis under unperturbed conditions. Through this mechanism of APC/C^{Cdh1} activation during G2 phase, cells can degrade and transcriptionally silence multiple cell-cycle proteins to allow cells to enter a state of senescence (Lee et al., 2009; Wiebusch and Hagemeier, 2010). The current work shows that P21 is not sufficient to enforce this arrest, because atypical repressor E2Fs also play a critical role. Potentially, these two routes can back each other up to ensure genomic integrity.

Multiple mechanisms could explain how DNA damage can activate E2F7/8 to mediate the cell-cycle arrest after completion of S phase. First, E2F7 is a direct transcriptional target of P53, meaning that E2F7 can act in parallel with P21, downstream of P53 (Aksoy et al., 2012; Carvajal et al., 2012). Second, we recently identified cyclin F as negative regulator of atypical E2Fs during G2 of unperturbed cell cycles (Yuan et al., 2019). Work from the Pagano lab showed that cyclin F is inactivated via ataxia telangiectasia mutated (ATM) in response to genotoxic damage (D'Angiolella et al., 2012). This cyclin F inactivation would then lead to reduced degradation of E2F7/8. Together these P53- and cyclin-F-dependent mechanisms could explain why E2F7/8 activity can accumulate in G2 cells after DNA damage to mediate a cell-cycle arrest.

Another major finding of the present study is that clearly not all arrested cells become senescent after DNA damage; many can escape this arrest to become tetraploid. Induction of senescence prevents proliferation of cells with damaged DNA (Baus et al., 2003; Krenning et al., 2014). Thus, this exit is believed to be an important first line of defense against tumor formation (Bartkova et al., 2005; Gire and Dulic, 2015). Stochastic oscillations in P53 could induce an escape from such an arrest,

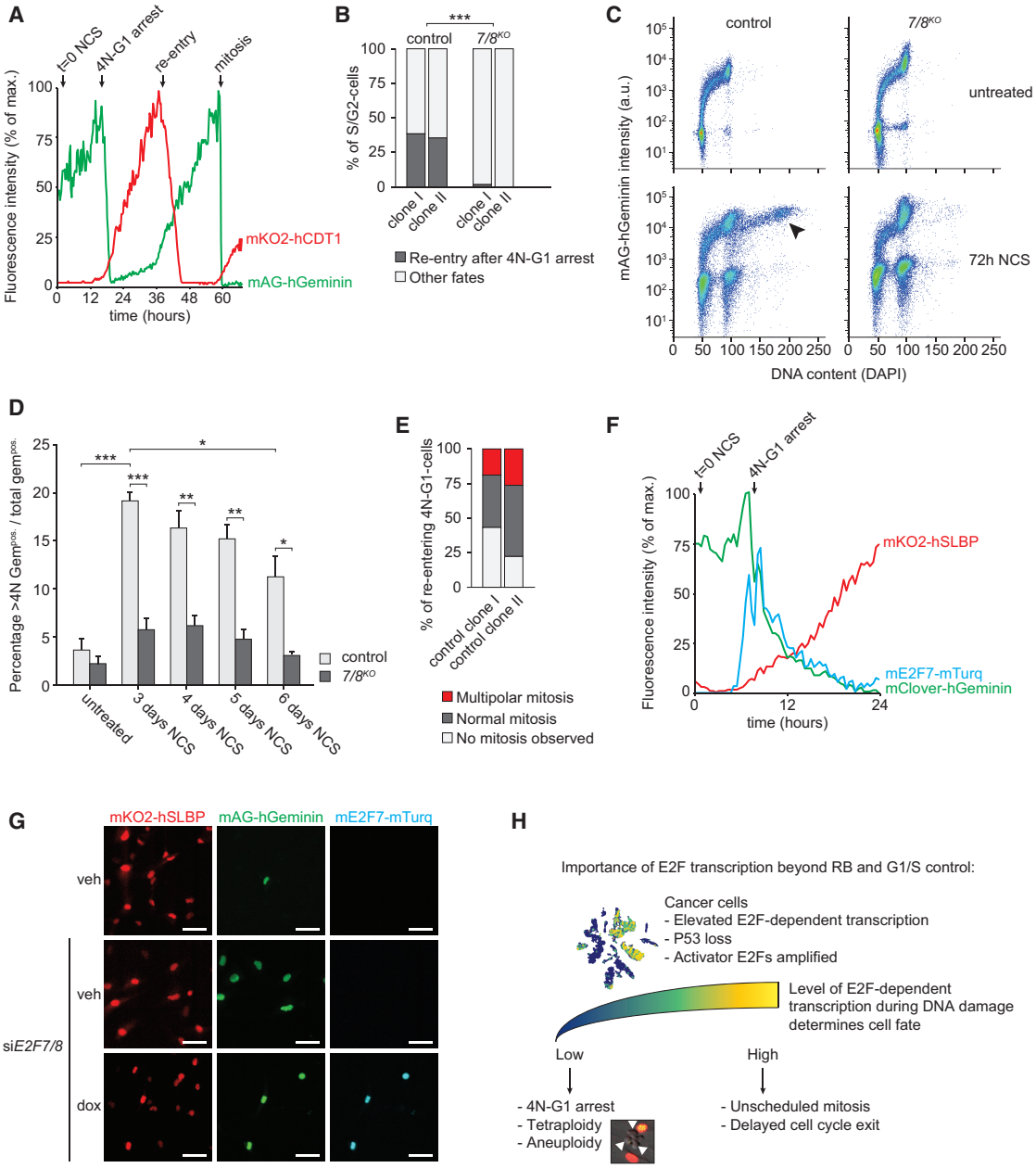

Figure 7. Endoreplication after Escape from DNA-Damage-Induced Arrest Are Blocked by E2F7/8 Deletion

(A) FUCCI fluorescence intensity over time in one representative control cell that underwent a 4N-G1 arrest and subsequently re-entered the cell cycle after ~2 days. Mitosis was confirmed by inspecting the differential interference contrast (DIC) images.

(B) Stacked bar graphs showing the percentages of S/G2 cells that re-entered the cell-cycle after a transient 4N-G1 arrest, seen by the re-emergence of geminin-mAG and disappearance of CDT1-mKO. Cell fates were determined by live-cell imaging over a period of 60 h. Per clone, n = 100 cells were followed. ***$p < 0.005$.

(C) Flow cytometry data showing DNA content and mAG-hGeminin expression in RPE cells before and 72 h after treatment with 100 ng/mL NCS. Arrowhead indicates population of 8N tetraploid G2 cells.

(D) Quantification of percentage >4N Gem^{pos} cells, measured by flow cytometry. Bars represent the average ± SEM.

(E) Quantification of the cell-cycle fates of control cells that re-entered the cell cycle after a transient 4N-G1 arrest upon treatment with 100 ng/mL NCS. Per clone, n = 50 cells were followed.

(F) Representative cell trace of a single cell overexpressing mTurquoise-tagged mouse E2F7, which entered a 4N-G1 arrest after 200 ng/mL NCS treatment in the presence of siE2F7/8. Doxycycline was added 2 h prior to NCS and became noticeable expressed ~6 h after NCS treatment. Both mAG-hGeminin and E2F7-mTurq are APC/C^{Cdh1} substrates and were degraded according to identical kinetics. In this cell line, mKO2-hCDT1 was replaced by mKO2-hSLBP.

(G) Snapshots of RPE-FUCCI cells 24 h after NCS treatment (200 ng/mL) in the presence or absence of siE2F7/8 and exogenous E2F7, showing that overexpressed E2F7 was only detectable in Gem^{pos} cells. Scale bar represents 50 μm.

(H) Schematic overview summarizing the main findings of the current study.

resulting in tetraploidy (Reyes et al., 2018). Tetraploidization precedes malignant transformation in various cancer types, and this escape could therefore potentially lead to oncogenic transformation (Davoli and de Lange, 2011; Tanaka et al., 2018). Tetraploidy is associated with the ability of non-transformed cells to form tumors in xenografted mice (Davoli and de Lange, 2012). In addition, tetraploidization may affect drug sensitivity of cells (Lee et al., 2011).

Importantly, *E2F7/8*^{KO} cells with elevated E2F transcription failed to become polyploid. Taking this into consideration, one could reason that prevention of tetraploidization by abnormally high E2F transcription could have a tumor-suppressing effect. However, our work shows that uncontrolled E2F target gene expression during S/G2 phase profoundly increased the number of unscheduled mitoses under DNA-damaging conditions. Unscheduled mitosis of diploid cells after DNA damage could be even more detrimental than the appearance of tetraploid cells. In the liver, for example, tetraploidization prevents formation of hepatocellular carcinoma, presumably because polyploid cells have a decreased risk to suffer loss of important tumor suppressor genes (Zhang et al., 2018). Liver-specific deletion of *E2f7/8* prevented polyploidization and promoted liver tumor growth, further supporting this notion (Chen et al., 2012; Kent et al., 2016; Pandit et al., 2012).

Although E2F7/8 and Emi1 are rarely mutated in cancer, we show now using single-cell transcriptomic data from human cancer patients that E2F-dependent transcription can be strongly induced in cycling malignant cells. This induction during S and G2 phase can occur via amplification of the activating E2F family member *E2F3*, as we show that overexpression of E2F3 elevates E2F target gene expression and precludes cell-cycle exit after DNA damage. Interestingly, *E2F3* is an oncogene, and its amplification drives proliferation and invasiveness of urinary bladder cancer (Oeggerli et al., 2004). Similarly, *E2F1* amplification or enhanced upstream transcription via *MYC* could elevate E2F-dependent transcription. This would then provide an important mechanism for cells to prevent undergoing a 4N-G1 arrest in response to DNA-damaging drugs. It should be noted that tumor cells with elevated E2F transcription would need to activate DNA repair mechanisms in order to prevent excessive DNA damage. Interestingly, many DNA repair pathways, such as mismatch repair, base excision repair, and homologous recombination, are all transcriptionally controlled by E2Fs. Future research will need to show which molecular mechanisms can establish heterogeneity in E2F transcription in cycling cancer cells and whether this plays a role in resistance to radiation or chemotherapeutic drugs.

STAR★METHODS

Detailed methods are provided in the online version of this paper and include the following:

- KEY RESOURCES TABLE
- RESOURCE AVAILABILITY
  - Lead Contact
  - Materials Availability
  - Data and Code Availability
- EXPERIMENTAL MODEL AND SUBJECT DETAILS
  - Cell lines and cell line generation
- METHOD DETAILS
  - RNAi transfections
  - Microscopy
  - Flow cytometry
  - Immunoblotting
  - Single cell RNA-sequencing
  - Analysis of public available datasets
  - Quantitative PCR
- QUANTIFICATION AND STATISTICAL ANALYSIS

SUPPLEMENTAL INFORMATION

Supplemental Information can be found online at https://doi.org/10.1016/j.celrep.2020.108449.

ACKNOWLEDGMENTS

We thank Judith Vivié and Mauro Muraro (Single Cell Discoveries, the Netherlands) for support with single-cell sequencing library preparation and sequencing services. Ger Arkesteijn (Faculty of Veterinary Medicine, Utrecht University, the Netherlands), Reinier van der Linden, and Stefan van der Elst (Hubrecht Institute-KNAW, the Netherlands) are thanked for assistance with FACS experiments. This work was financially supported by the China Scholarship Council (CSC; file 201306380101 to R.Y.), KWF Kankerbestrijding (Dutch Cancer Society project grants UU2013-5777 and 11941-2018-II), and ZonMw (grant 91116011). Further financial support was provided by a research infrastructure grant from Utrecht Life Sciences.

AUTHOR CONTRIBUTIONS

H.A.S. conceived and performed experiments, analyzed data, and wrote the manuscript. L.M.v.R., E.M., E.A.v.L, and R.Y. conceived, analyzed, and performed experiments and analyzed data. F.M.R. performed bioinformatic analysis. R.W. provided expert support with live-cell imaging experiments and data analysis. A.d.B. provided mentorship and wrote the manuscript. B.W. conceived and oversaw the study, analyzed data, and wrote the manuscript.

DECLARATION OF INTERESTS

The authors declare no competing interests.

Received: March 30, 2020
Revised: August 26, 2020
Accepted: November 9, 2020
Published: December 1, 2020

REFERENCES

Aksoy, O., Chicas, A., Zeng, T., Zhao, Z., McCurrach, M., Wang, X., and Lowe, S.W. (2012). The atypical E2F family member E2F7 couples the p53 and RB pathways during cellular senescence. Genes Dev. *26*, 1546–1557.

Arora, M., Moser, J., Phadke, H., Basha, A.A., and Spencer, S.L. (2017). Endogenous replication stress in mother cells leads to quiescence of daughter cells. Cell Rep. *19*, 1351–1364.

Bajar, B.T., Lam, A.J., Badiee, R.K., Oh, Y.H., Chu, J., Zhou, X.X., Kim, N., Kim, B.B., Chung, M., Yablonovitch, A.L., et al. (2016). Fluorescent indicators for simultaneous reporting of all four cell cycle phases. Nat. Methods *13*, 993–996.

Bartkova, J., Horejsí, Z., Koed, K., Krämer, A., Tort, F., Zieger, K., Guldberg, P., Sehested, M., Nesland, J.M., Lukas, C., et al. (2005). DNA damage response as a candidate anti-cancer barrier in early human tumorigenesis. Nature *434*, 864–870.

Bassermann, F., Frescas, D., Guardavaccaro, D., Busino, L., Peschiaroli, A., and Pagano, M. (2008). The Cdc14B-Cdh1-Plk1 axis controls the G2 DNA-damage-response checkpoint. Cell *134*, 256–267.

Baus, F., Gire, V., Fisher, D., Piette, J., and Dulić, V. (2003). Permanent cell cycle exit in G2 phase after DNA damage in normal human fibroblasts. EMBO J. *22*, 3992–4002.

Bertoli, C., Skotheim, J.M., and de Bruin, R.A. (2013). Control of cell cycle transcription during G1 and S phases. Nat. Rev. Mol. Cell Biol. *14*, 518–528.

Bertoli, C., Herlihy, A.E., Pennycook, B.R., Kriston-Vizi, J., and de Bruin, R.A.M. (2016). Sustained E2F-dependent transcription is a key mechanism to prevent replication-stress-induced DNA damage. Cell Rep. *15*, 1412–1422.

Boekhout, M., Yuan, R., Wondergem, A.P., Segeren, H.A., van Liere, E.A., Awol, N., Jansen, I., Wolthuis, R.M., de Bruin, A., and Westendorp, B. (2016). Feedback regulation between atypical E2Fs and APC/CCdh1 coordinates cell cycle progression. EMBO Rep. *17*, 414–427.

Butler, A., Hoffman, P., Smibert, P., Papalexi, E., and Satija, R. (2018). Integrating single-cell transcriptomic data across different conditions, technologies, and species. Nat. Biotechnol. *36*, 411–420.

Cappell, S.D., Chung, M., Jaimovich, A., Spencer, S.L., and Meyer, T. (2016). Irreversible APC(Cdh1) Inactivation Underlies the Point of No Return for Cell-Cycle Entry. Cell *166*, 167–180.

Carvajal, L.A., Hamard, P.J., Tonnessen, C., and Manfredi, J.J. (2012). E2F7, a novel target, is up-regulated by p53 and mediates DNA damage-dependent transcriptional repression. Genes Dev. *26*, 1533–1545.

Chao, H.X., Poovey, C.E., Privette, A.A., Grant, G.D., Chao, H.Y., Cook, J.G., and Purvis, J.E. (2017). Orchestration of DNA damage checkpoint dynamics across the human cell cycle. Cell Syst. *5*, 445–459.e5.

Chen, H.Z., Ouseph, M.M., Li, J., Pécot, T., Chokshi, V., Kent, L., Bae, S., Byrne, M., Duran, C., Comstock, G., et al. (2012). Canonical and atypical E2Fs regulate the mammalian endocycle. Nat. Cell Biol. *14*, 1192–1202.

D'Angiolella, V., Donato, V., Forrester, F.M., Jeong, Y.T., Pellacani, C., Kudo, Y., Saraf, A., Florens, L., Washburn, M.P., and Pagano, M. (2012). Cyclin F-mediated degradation of ribonucleotide reductase M2 controls genome integrity and DNA repair. Cell *149*, 1023–1034.

Davoli, T., and de Lange, T. (2011). The causes and consequences of polyploidy in normal development and cancer. Annu. Rev. Cell Dev. Biol. *27*, 585–610.

Davoli, T., and de Lange, T. (2012). Telomere-driven tetraploidization occurs in human cells undergoing crisis and promotes transformation of mouse cells. Cancer Cell *21*, 765–776.

Dobin, A., Davis, C.A., Schlesinger, F., Drenkow, J., Zaleski, C., Jha, S., Batut, P., Chaisson, M., and Gingeras, T.R. (2013). STAR: ultrafast universal RNA-seq aligner. Bioinformatics *29*, 15–21.

Gire, V., and Dulic, V. (2015). Senescence from G2 arrest, revisited. Cell Cycle *14*, 297–304.

Hafemeister, C., and Satija, R. (2019). Normalization and variance stabilization of single-cell RNA-seq data using regularized negative binomial regression. Genome Biol. *20*, 296–1.

Helmbold, H., Kömm, N., Deppert, W., and Bohn, W. (2009). Rb2/p130 is the dominating pocket protein in the p53-p21 DNA damage response pathway leading to senescence. Oncogene *28*, 3456–3467.

Kent, L.N., and Leone, G. (2019). The broken cycle: E2F dysfunction in cancer. Nat. Rev. Cancer *19*, 326–338.

Kent, L.N., Rakijas, J.B., Pandit, S.K., Westendorp, B., Chen, H.Z., Huntington, J.T., Tang, X., Bae, S., Srivastava, A., Senapati, S., et al. (2016). E2f8 mediates tumor suppression in postnatal liver development. J. Clin. Invest. *126*, 2955–2969.

Krenning, L., Feringa, F.M., Shaltiel, I.A., van den Berg, J., and Medema, R.H. (2014). Transient activation of p53 in G2 phase is sufficient to induce senescence. Mol. Cell *55*, 59–72.

Lan, W., Bian, B., Xia, Y., Dou, S., Gayet, O., Bigonnet, M., Santofimia-Castano, P., Cong, M., Peng, L., Dusetti, N., and Iovanna, J. (2018). E2F signature is predictive for the pancreatic adenocarcinoma clinical outcome and sensitivity to E2F inhibitors, but not for the response to cytotoxic-based treatments. Sci. Rep. *1*, 8330-z.

Lee, J., Kim, J.A., Barbier, V., Fotedar, A., and Fotedar, R. (2009). DNA damage triggers p21WAF1-dependent Emi1 down-regulation that maintains G2 arrest. Mol. Biol. Cell *20*, 1891–1902.

Lee, A.J., Endesfelder, D., Rowan, A.J., Walther, A., Birkbak, N.J., Futreal, P.A., Downward, J., Szallasi, Z., Tomlinson, I.P., Howell, M., et al. (2011). Chromosomal instability confers intrinsic multidrug resistance. Cancer Res. *71*, 1858–1870.

Li, J., Ran, C., Li, E., Gordon, F., Comstock, G., Siddiqui, H., Cleghorn, W., Chen, H.Z., Kornacker, K., Liu, C.G., et al. (2008). Synergistic function of E2F7 and E2F8 is essential for cell survival and embryonic development. Dev. Cell *14*, 62–75.

Lukas, C., Sørensen, C.S., Kramer, E., Santoni-Rugiu, E., Lindeneg, C., Peters, J.M., Bartek, J., and Lukas, J. (1999). Accumulation of cyclin B1 requires E2F and cyclin-A-dependent rearrangement of the anaphase-promoting complex. Nature *401*, 815–818.

Moreno, E., Toussaint, M.J.M., van Essen, S.C., Bongiovanni, L., van Liere, E.A., Koster, M.H., Yuan, R., van Deursen, J., Westendorp, B., and de Bruin, A. (2020). E2F7 is a potent inhibitor of liver tumor growth in adult mice. Hepatology.

Muraro, M.J., Dharmadhikari, G., Grün, D., Groen, N., Dielen, T., Jansen, E., van Gurp, L., Engelse, M.A., Carlotti, F., de Koning, E.J., and van Oudenaarden, A. (2016). A single-cell transcriptome atlas of the human pancreas. Cell Syst. *3*, 385–394.e3.

Oeggerli, M., Tomovska, S., Schraml, P., Calvano-Forte, D., Schafroth, S., Simon, R., Gasser, T., Mihatsch, M.J., and Sauter, G. (2004). E2F3 amplification and overexpression is associated with invasive tumor growth and rapid tumor cell proliferation in urinary bladder cancer. Oncogene *23*, 5616–5623.

Pandit, S.K., Westendorp, B., Nantasanti, S., van Liere, E., Tooten, P.C., Cornelissen, P.W., Toussaint, M.J., Lamers, W.H., and de Bruin, A. (2012). E2F8 is essential for polyploidization in mammalian cells. Nat. Cell Biol. *14*, 1181–1191.

Puram, S.V., Tirosh, I., Parikh, A.S., Patel, A.P., Yizhak, K., Gillespie, S., Rodman, C., Luo, C.L., Mroz, E.A., Emerick, K.S., et al. (2017). Single-cell transcriptomic analysis of primary and metastatic tumor ecosystems in head and neck cancer. Cell *171*, 1611–1624.e24.

R Core Team (2019). R: A language and environment for statistical computing (Vienna, Austria: R Foundation for Statistical Computing). https://www.R-project.org/.

Reyes, J., Chen, J.Y., Stewart-Ornstein, J., Karhohs, K.W., Mock, C.S., and Lahav, G. (2018). Fluctuations in p53 Signaling Allow Escape from Cell-Cycle Arrest. Mol. Cell *71*, 581–591.e5.

RStudio Team (2020). RStudio: Integrated Development for R. RStudio (Boston, MA: PBC). http://www.rstudio.com/.

Saenz-Ponce, N., Pillay, R., de Long, L.M., Kashyap, T., Argueta, C., Landesman, Y., Hazar-Rethinam, M., Boros, S., Panizza, B., Jacquemyn, M., et al. (2018). Targeting the XPO1-dependent nuclear export of E2F7 reverses anthracycline resistance in head and neck squamous cell carcinomas. Sci. Transl. Med. *447*, eaar7223.

Sakaue-Sawano, A., Kurokawa, H., Morimura, T., Hanyu, A., Hama, H., Osawa, H., Kashiwagi, S., Fukami, K., Miyata, T., Miyoshi, H., et al. (2008). Visualizing spatiotemporal dynamics of multicellular cell-cycle progression. Cell *132*, 487–498.

Stevens, M., Oomens, L., Broekmaat, J., Weersink, J., Abali, F., Swennenhuis, J., and Tibbe, A. (2018). VyCAP's puncher technology for single cell identification, isolation, and analysis. Cytometry A *93*, 1255–1259.

Tanaka, K., Goto, H., Nishimura, Y., Kasahara, K., Mizoguchi, A., and Inagaki, M. (2018). Tetraploidy in cancer and its possible link to aging. Cancer Sci. *109*, 2632–2640.

Thurlings, I., Martínez-López, L.M., Westendorp, B., Zijp, M., Kuiper, R., Tooten, P., Kent, L.N., Leone, G., Vos, H.J., Burgering, B., and de Bruin, A. (2017).

Synergistic functions of E2F7 and E2F8 are critical to suppress stress-induced skin cancer. Oncogene *36*, 829–839.

Trapnell, C., Cacchiarelli, D., Grimsby, J., Pokharel, P., Li, S., Morse, M., Lennon, N.J., Livak, K.J., Mikkelsen, T.S., and Rinn, J.L. (2014). The dynamics and regulators of cell fate decisions are revealed by pseudotemporal ordering of single cells. Nat. Biotechnol. *32*, 381–386.

van Galen, P., Hovestadt, V., Wadsworth Ii, M.H., Hughes, T.K., Griffin, G.K., Battaglia, S., Verga, J.A., Stephansky, J., Pastika, T.J., Lombardi Story, J., et al. (2019). Single-cell RNA-seq reveals AML hierarchies relevant to disease progression and immunity. Cell *176*, 1265–1281.e24.

Westendorp, B., Mokry, M., Groot Koerkamp, M.J., Holstege, F.C., Cuppen, E., and de Bruin, A. (2012). E2F7 represses a network of oscillating cell cycle genes to control S-phase progression. Nucleic Acids Res. *40*, 3511–3523.

Wiebusch, L., and Hagemeier, C. (2010). p53- and p21-dependent premature APC/C-Cdh1 activation in G2 is part of the long-term response to genotoxic stress. Oncogene *29*, 3477–3489.

Yuan, R., Liu, Q., Segeren, H.A., Yuniati, L., Guardavaccaro, D., Lebbink, R.J., Westendorp, B., and de Bruin, A. (2019). Cyclin F-dependent degradation of E2F7 is critical for DNA repair and G2-phase progression. EMBO J. *38*, e101430.

Zhang, S., Zhou, K., Luo, X., Li, L., Tu, H.C., Sehgal, A., Nguyen, L.H., Zhang, Y., Gopal, P., Tarlow, B.D., et al. (2018). The polyploid state plays a tumor-suppressive role in the liver. Dev. Cell *44*, 447–459.e5.

STAR★METHODS

KEY RESOURCES TABLE

REAGENT or RESOURCE	SOURCE	IDENTIFIER
Antibodies		
Mouse monoclonal anti-CDC6	Santa Cruz Biotechnology	Cat # sc-9964; RRID: AB_627236
Rabbit monoclonal anti CHK1, phospho(Ser345)	Cell Signaling Technology	Cat# 2348; RRID: AB_331212
Mouse monoclonal anti-CHK1	Cell Signaling Technology	Cat# 2360; RRID: AB_2080320
Mouse monoclonal anti-E2F3 (PG30)	Santa Cruz Biotechnology	Cat# sc-56665; RRID: AB_1122397
Mouse monoclonal anti-Emi1 (FBXO5)	Thermo Fisher	Cat# 37-6600; RRID: AB_2533333
Goat anti-GFP (used for mTurquoise detection)	Abcam	Cat# ab6673; RRID: AB_305643
Rabbit polyclonal anti-P21	Santa Cruz Biotechnology	Cat# sc-471; RRID: AB_632123
Mouse monoclonal anti-P53	Millipore	Cat# OP03; RRID: AB_2335865
Rabbit polyclonal anti-Rb	Santa Cruz Biotechnology	Cat# sc-50; RRID: AB_632339
Mouse monoclonal anti-gamma-Tubulin	Sigma-Aldrich	Cat# T6557; RRID: AB_477584
Rabbit anti-Phospho-Histone H2A.X (Ser139)	Cell Signaling Technology	Cat# 2577; RRID: AB_2118010
Rabbit anti-phospho-Histone H3 (Ser10)	Millipore	Cat# 06-570; RRID: AB_310177
Chemicals, Peptides, and Recombinant Proteins		
CDK4/6 inhibitor PD-0332991 (Palbociclib)	Selleck Chemicals	Cat# S1116
WEE1 inhibitor MK-1775 (Adavosertib)	Selleck Chemicals	Cat# S1525
Neocarzinostatin	Sigma-Aldrich	Cat# N9162
Protease inhibitor cocktail	Sigma-Aldrich	Cat# 11873580001
Vybrant DiD Cell-labeling solution	Thermo Fisher	Cat# V22887
Vybrant Dye Cycle violet	Thermo Fisher	Cat# V35003
Fetal bovine serum	Thermo Fisher	Cat# 10500064
DMEM	Thermo Fisher	Cat# 41966052
Critical Commercial Assays		
RNeasy Mini Kit for RNA extraction	QIAGEN	Cat# 74106
Click-iT Plus Alexa Fluor 647 Flow cytometry assay kit	Thermo Fisher	Cat# C10634
Deposited Data		
Single cell RNA-sequencing RPE-FUCCI cells	This paper	GEO: GSE146759
Single cell RNA-sequencing human HNSCC	Puram et al., 2017	GEO: GSE103322
Single cell RNA-sequencing human AML	van Galen et al., 2019	GEO: GSE116256
Experimental Models: Cell Lines		
hTert-RPE1	ATCC	Cat# CRL-4000; RRID:CVCL_4388
hTert-RPE1-FUCCI	Boekhout et al., 2016	N/A
hTert-RPE1-FUCCI-*E2F7/8*^{KO}	Yuan et al., 2019	N/A
hTert-RPE1-FUCCI-TetR/E2F3mTurq	This paper	N/A
hTert-RPE1-FUCCI-TetR/E2F7mTurq	This paper	N/A
HEK293T cells	ATCC	Cat# 300192/p777_HEK293; RRID:CVCL_0045
Oligonucleotides		
For primers used for qPCR, see Table S1	This paper	N/A
Scrambled siRNA	Dharmacon	Cat# D-001210-02-05

(*Continued on next page*)

CellPress
OPEN ACCESS

Continued

REAGENT or RESOURCE	SOURCE	IDENTIFIER
Human P53 siRNA	Dharmacon	Cat# LQ-003329-00-0002
Human RB1 siRNA	Dharmacon	Cat# LQ-003296-02-0002
Human FBXO5 (Emi1) siRNA	Dharmacon	Cat# L-012434-00-0020
Human CDK1 siRNA	Dharmacan	Cat# L-003224-00-0005
Human CDK2 siRNA	Dharmacon	Cat# L-003236-00-0005
Human E2F7 siRNA	Thermo Fisher	Cat# HSS175354
Human E2F8 siRNA	Thermo Fisher	Cat# HSS128758/HSS128760
sgRNA targeting hE2F7 1: GTGCTGCCAGCCCAGATATA	Yuan et al., 2019	N/A
sgRNA targeting hE2F7 2: GAGCTAGAAACTTCTGGCAC	Yuan et al., 2019	N/A
sgRNA targeting hE2F8 1: GTTCCTCTGCCACTTCGTCA	Yuan et al., 2019	N/A
sgRNA targeting hE2F8 2: GATCTCTGTTGCGGATCTCA	Yuan et al., 2019	N/A
Recombinant DNA		
Apple-53BP1trunc	Addgene	RRID:Addgene_69531
pLenti CMV TetR Blast (716-1)	Addgene	RRID:Addgene_17492
pLenti CMV/TO Puro – hE2F3-mTurquoise	This paper	N/A
pLenti CMV/TO Puro – mE2F7-mTurquoise	This paper	N/A
Clover-Geminin(1-110)	Addgene	RRID:Addgene_83915
mKO2-SLBP(18-126)	Addgene	RRID:Addgene_83914
pMDLg/pRRE lentiviral packaging	Addgene	RRID:Addgene_12251
pRSV-Rev lentiviral packaging	Addgene	RRID:Addgene_12253
pCMV-VSV-G lentiviral packaging	Addgene	RRID:Addgene_8454
Software and Algorithms		
FIJI (ImageJ)	https://fiji.sc	RRID: SCR_002285
TrackMate	https://imagej.net/TrackMate	N/A
Custom VyCAP image quantification macro	This paper	N/A
NIS Elements	Nikon	RRID: SCR_014329
FlowJo	BD	RRID: SCR_008520
STAR sequencing aligner	https://github.com/alexdobin/STAR	RRID: SCR_015899
RStudio	https://www.rstudio.com/	RRID: SCR_000432
Seurat	https://satijalab.org/seurat/get_started.html	RRID: SCR_016341
Monocle	https://cole-trapnell-lab.github.io/monocle3	RRID: SCR_018685

RESOURCE AVAILABILITY

Lead Contact

Further information and requests for resources and reagents should be directed to Bart Westendorp (b.westendorp@uu.nl).

Materials Availability

All materials newly generated in this study are available from the Lead Contact with appropriate regulatory clearances and a completed Materials Transfer Agreement.

Data and Code Availability

Raw and processed single cell RNA-sequencing data generated in this study are available on Gene Expression Omnibus under accession number GSE146759.

EXPERIMENTAL MODEL AND SUBJECT DETAILS

Cell lines and cell line generation

RPE1- hTERT (female origin) and HEK293T (female fetus) cell lines were purchased from ATCC and cultured in DMEM (41966052; Thermo Fisher Scientific) containing 10% fetal bovine serum (10500064; Thermo Fisher Scientific) at 37°C. Neocarzinostatin was purchased from Sigma-Aldrich (N9162). Palbociclib (S1116) and Adavosertib (S1525) were purchased from Selleckchem and used at final concentrations of 1.0 μM and 2.5 μM respectively.

The strategy to produce E2F7/8 double mutant RPE cell lines and confirmation of deletion are described in Yuan et al. (2019). Briefly, cells were transduced with a lentiviral expression vector encoding both Flag-tagged Cas9 and a single guide (sg) RNA sequence against E2F7 (sgRNA #1: GTGCTGCCAGCCCAGATATA, sgRNA #2: GAGCTAGAAACTTCTGGCAC) or E2F8 (sgRNA #1: GTTCCTCTGCCACTTCGTCA, sgRNA #2: GATCTCTGTTGCGGATCTCA). Lentiviral particles were produced by co-transfecting the constructs with third-generation packaging plasmids into HEK 239T cells. The sgE2F7 and sgE2F8 vectors contained puromycin and blasticidin resistance cassettes, respectively, thus allowing for sequential selection of E2F7 and E2F8 mutant clones by manual picking. Cells expressing the vector containing only Cas9, but no sgRNA, served as control cell lines.

The lentiviral construct containing a truncated version of 53BP1 tagged with mApple was a gift from Ralph Weissleder (Addgene plasmid # 69531; http://addgene.org/69531; RRID:Addgene_69531), fluorescent tag was changed to mTurquoise2 using Gibson Assembly.

Inducible E2F3 and E2F7-mTurquoise2 tagged RPE cell lines were created as previously described (Moreno et al., 2020). Briefly, plasmids with murine E2F7 or human E2F3 and mTurquoise2 tag were created using Gibson Assembly. Next, lentiviral plasmids containing the Tet repressor and desired genes were introduced in RPE cells harboring the Fucci4 system using the third generation lentiviral packaging plasmids. The lentiviral constructs encoding the Fucci4 system (Clover-Geminin(1-110) and mKO2-SLBP(18-126)) were a gift from Michael Lin (Addgene plasmid # 83915 ; http://addgene.org/83915; RRID:Addgene_83915 and Addgene plasmid # 83914 ; http://addgene.org/83914; RRID:Addgene_83914).

Lentivirus was produced by transfecting HEK293T cells with 10 μg lentiviral packaging plasmids (1:1:1) and 10 μg of the desired construct with PEI for 2 hours. Then, 10 mL fresh medium was added and virus was harvested after 48 hours. Three milliliters of virus containing medium and polybrene (8 μg/ml) was added to RPE cells for an incubation of 24 hours. RPE cells containing the construct were selected with puromycin (1.0 μg/ml) for 5 days.

METHOD DETAILS

RNAi transfections

For siRNA experiments, RPE cells were transfected, unless stated otherwise, with a final concentration of 10nM siRNA and 2uL/ml RNAiMAX reagent used according to the manufacturers' instructions (Life Technologies, 13778030). The following siRNAs were used: Dharmacon D-001210-02-05 (Scrambled), LQ-003329-00-0002 (siTP53), LQ-003296-02-0002 (siRB1), L-012434-00-0020 (siFBXO5) L-003236-00-0005 (siCDK2) and L-003224-00-0005 (siCDK1), Thermo Fisher HSS175354 (siE2F7) and HSS128758/ HSS128760 (siE2F8).

Microscopy

For live cell imaging, 1000 RPE cells were seeded into a 8-well μ-slide (Ibidi). Images were acquired every 20 minutes for 72 hours on a Nikon A1R-STORM microscope using a 10x objective in a humidified chamber at 37°C, 5% CO_2. For live cell imaging experiments with 53BP1-mTurquoise2 tagged cell lines, Adavosertib, or inducible E2F3/7, 5000 cells were plated in a CELLview slide (Greiner) and a 20x objective with 1.5x zoom was used. Cell tracking was performed manually and in a semi-automated manner using the FIJI plugin Trackmate. Subsequently, fluorescent intensity of CDT1-mKusabira Orange (mKO) and Geminin-mAzami Green (mAG) in these ROIs (region of interest) was automatically measured using NIS Elements software and FIJI. A cell was considered Geminin or CDT1 positive if the signal in three consecutive frames was higher than 10% of the maximum. Cell cycle phases were assigned, G1-phase: CDT1 positive, early S-phase: CDT1 and Geminin positive and late S/G2-phase: Geminin positive. Mitosis was determined by nuclear envelop breakdown and observation of cell division using the DIC (differential interference contrast) image.

VyCAP microscopic images were quantified with an in-house built ImageJ macro. Images of each punched cell, stored in folders labeled according to plateID and well ID are recursively quantified by creating a ROI in the Hoechst image, and subsequent measurement of FUCCI fluorescence (cell cycle) and DiD fluorescence (*E2F7/8*^{KO} versus control). The outputs of these quantifications were then merged in Rstudio to create a metadata file.

Images for 53BP1 foci analysis were acquired on a Ti-E microscope (Nikon, Japan). ROIs were created using an overlay of the CDT1-mKO and Geminin-mAG channel using an in-house built ImageJ macro. Fluorescent intensity of CDT1-mKO and Geminin-mAG and 53BP1 foci per ROI were analyzed in a semi-automated manner in ImageJ. A cell was considered Geminin or CDT1 positive if the signal was higher than 10% of the maximum.

For immunofluorescence staining, cells were seeded on coverslips. For γH2AX staining cells were treated for 1 minute with 0.2% ice-cold Triton X-100 prior to fixation. Then cells were fixed with 4% PFA for 20 minutes and permeabilized with 0.1% Trition X-100 for 1 minute at room temperature. Cells were blocked using 5% goat serum (γH2AX) or 4% BSA (pH3) and treated with primary

antibodies, secondary antibodies and DAPI (Sigma-Aldrich). Subsequently, coverslips were mounted and analyzed on a Leica SPE-II (DMI4000) microscope. For each image ROIs were determined based on DAPI signal and γH2AX foci per cell were quantified using the Find Maxima function in a custom made ImageJ macro. At least 4 different images and 250 cells per condition were analyzed. Antibodies used are listed in Table S2.

Flow cytometry

For FACS sorting experiments cells were resuspended in DMEM. Sorting was performed based on Geminin-mAG, CDT1-mKO2, and Vybrant Dye Cycle violet (V35003, Thermo Fisher) signal on a BD-influx or BD-Fusion. For RNA analysis 50.000 cells per condition were collected in PBS.

For DNA content and fluorescent intensity analysis, cells were harvested by trypsinization and subsequent fixated with 70% ethanol and overnight storage at 4°C. Before staining, cells were washed twice with ice-cold Tris-buffered saline (TBS) and re-suspended in 500 μL staining buffer that contained 0.25 μg/ml DAPI (F6057; Sigma-Aldrich), 250 μg/ml RNase A (RNASEA-RO; Roche), and 0.1% bovine serum albumin (A8531; Sigma-Aldrich). For EdU labeling experiments, cells were pulsed with 10 μM EdU. Fixation and click-it procedure was performed using the Click-iT Plus Alexa Fluor 647 Flow cytometry assay kit according to manufacturer's instructions (C10634, Thermo Fisher).

Samples were loaded on a BD FACS Canto II or Beckman CytoFLEX flow cytometer. Quantification of ploidy and Geminin positivity were conducted using FlowJo v10.0 software.

Immunoblotting

For immunoblotting cells were lysed in ice-cold RIPA-buffer (50nM Tris-HCl pH 7.5, 1mM EDTA, 150mM NaCl, 0.25% deoxycholate, 1% NP-40) supplemented with 1mM NaF, 1mM NaV_3O_4 and protease inhibitor cocktail (11873580001, Sigma Aldrich) after which was proceeded to a standard SDS-page immunoblot. Antibodies used and dilutions are listed in Table S2.

Single cell RNA-sequencing

For each experiment, either control or *E2F7/8*^{KO} cells were labeled with DiD Vybrant dye (ThermoFisher), to distinguish between those two genotypes. After trypsinization, mutant and control cells were resuspended 1:1 in 1 mL of serum-free DMEM containing 1:20000 Hoechst33342 dye (ThermoFisher), and loaded on a VyCAP chip (VyCAP B.V. the Netherlands). The entire chip was scanned on a Ti-E microscope (Nikon, Japan) using the following filter cubes from Chroma; 49000 (Hoechst 33342), 49002 (Geminin-mAG), 49004 (CDT1-mKO), 49006 (DiD).

Using custom VyCAP software we then randomly selected wells containing one cell (detected by Hoechst signal) to punch into 384-well plates. These plates contain 100 nL of barcoded CEL-Seq2 primers + dNTPS, which was protected from evaporation by 5 μL mineral oil. After punching, the plates were covered with adhesive foil, centrifuged for 1 minute at 2500 G, and immediately stored at −80° until further processing.

The library preparations, Illumina sequencing, and read alignment to the human genome (Hg19) were performed by Single Cell Discoveries as described before (Muraro et al., 2016). The mapped reads were counted using STAR (Dobin et al., 2013) and then further processed in Rstudio (version 1.2.5019; RStudio Team, 2020) and R (version 3.6.1; R Core Team, 2019) using the Seurat package (Butler et al., 2018). Cells expressing < 1000 or > 10000 genes, < 4000 Unique Molecular Identifier (UMI) counts, and > 30 percent mitochondrial genes where filtered out. Next, data where normalized and scaled with the SCTransform method (Hafemeister and Satija, 2019), and principle component analysis was used for dimension reduction. Based on the elbow plot, only the first six principle components where used for the clustering analysis. Clusters were visualized with t-Distributed Stochastic Neighbor Embedding (t-SNE). Differentially expressed genes between clusters were obtained using a parametric Wilcoxon rank sum test at a significance level of $p < 0.05$. Additionally, pseudo time analysis was performed with the Monocle package (Trapnell et al., 2014).

Analysis of public available datasets

Normalized count data and metadata from studies GSE103322 (head and neck squamous cell carcinoma) and GSE116256 (acute myeloid leukemia) were downloaded from Gene Expression Omnibus. Data were processed using the Seurat package as described above. E2F scores were obtained by calculating mean z-scores for a panel of 80 E2F target genes. The methodology to determine cell type identities, classification into malignant versus normal cells, and classification into cycling versus non-cycling cells are described in detail in the original publications (Puram et al., 2017; van Galen et al., 2019). From study GSE116256 we included only samples from patients prior to treatment, and with unambiguous malignancy classifications (12 out of 16). Statistical analysis of E2F scores between various normal and malignant cells was performed using a Kruskall-Wallis test followed by Dunn's test of multiple comparisons, with Benjamini-Hochberg post hoc *P*-value correction.

Quantitative PCR

Isolation of RNA, cDNA synthesis, and quantitative PCR were performed based on the manufacturers' instructions for QIAGEN (RNeasy Kits), Thermo Fisher Scientific (cDNA synthesis Kits), and Bio-Rad (SYBR Green Master Mix), respectively. Gene transcript levels were determined using the ΔΔCt method for multiple-reference gene correction. *GAPDH* and *RSP18* were used as reference genes for normalization. qPCR primer sequences are provided in Table S1.

QUANTIFICATION AND STATISTICAL ANALYSIS

Immunoblot, flow cytometry, and qPCR results were repeated four times unless otherwise described in the figure legends. Statistical analyses on qPCR was done by a Student's t test for Figures 2A, 5G, 5I, S4G, and S4H and a Kruskal-Wallis test with a post hoc Dunnett's test for Figures 4E, 5B, 6D, S7D, S9E, and S9F. Cumulative curves from Figures 2B, 2F, 3G, 3D, and S5E were analyzed by log-rank tests.

* $p < 0.05$, ** $p < 0.01$, ***$p < 0.001$ unless indicated otherwise. Sample sizes and other experiment-specific statistical details are described in the figure legends.